

Image Matching Across Wide Baselines: From Paper to Practice

Yuhe Jin · Dmytro Mishkin · Anastasiia Mishchuk · Jiri Matas · Pascal Fua ·
Kwang Moo Yi · Eduard Trulls

Received: date / Accepted: date

Abstract We introduce a comprehensive benchmark for local features and robust estimation algorithms, focusing on the downstream task – the accuracy of the reconstructed camera pose – as our primary metric. Our pipeline’s modular structure allows us to easily integrate, configure, and combine different methods and heuristics. We demonstrate this by embedding dozens of popular algorithms and evaluating them, from seminal works to the cutting edge of machine learning research. We show that with proper settings, classical solutions may still outperform the *perceived* state of the art.

Besides establishing the *actual* state of the art, the experiments conducted in this paper reveal unexpected properties of Structure from Motion (SfM) pipelines that can

This work was partially supported by the Natural Sciences and Engineering Research Council of Canada (NSERC) Discovery Grant “Deep Visual Geometry Machines” (RGPIN-2018-03788), by systems supplied by Compute Canada, and by Google’s Visual Positioning Service. DM and JM were supported by OP VVV funded project CZ.02.1.01/0.0/0.0/16 019/0000765 “Research Center for Informatics”. DM was also supported by CTU student grant SGS17/185/OHK3/3T/13 and by the Austrian Ministry for Transport, Innovation and Technology, the Federal Ministry for Digital and Economic Affairs, and the Province of Upper Austria in the frame of the COMET center SCCH. AM was supported by the Swiss National Science Foundation.

Y. Jin, K.M. Yi
Visual Computing Group, University of Victoria
E-mail: {yuhejin, kyj}@uvic.ca

A. Mishchuk, P. Fua
Computer Vision Lab, École Polytechnique Fédérale de Lausanne
E-mail: {anastasiia.mishchuk, pascal.fua}@epfl.ch

D. Mishkin, J. Matas
Center for Machine Perception, Czech Technical University, Prague
E-mail: {mishkdmy, matas}@cmp.felk.cvut.cz

E. Trulls
Google Research
E-mail: trulls@google.com

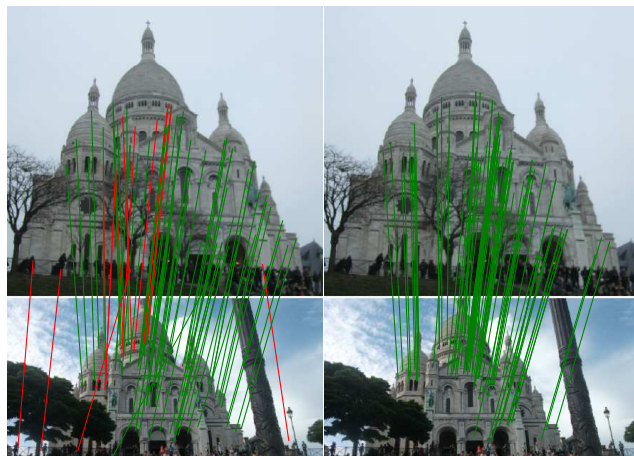


Fig. 1 Every paper claims to outperform the state of the art. Is this possible, or an artifact of insufficient validation? On the left, we show stereo matches obtained with **D2-Net** (2019) [38], a state-of-the-art local feature, using OpenCV RANSAC with its default settings. We color the inliers in green if they are correct and in red otherwise. On the right, we show **SIFT** (1999) [55] with a carefully tuned MAGSAC [32] – notice how the latter performs much better. This illustrates our take-home message: to correctly evaluate a method’s performance, it needs to be embedded within the pipeline used to solve a given problem, and the different components in said pipeline need to be tuned carefully and jointly, which requires engineering and domain expertise. We fill this need with a new, modular benchmark for sparse image matching, incorporating dozens of built-in methods.

be exploited to help improve their performance, for both algorithmic and learned methods. Data and code are online¹, providing an easy-to-use and flexible framework for the benchmarking of local feature and robust estimation methods, both *alongside* and *against* top-performing methods. This work provides the basis for an open challenge on wide-baseline image matching².

¹ <https://github.com/vcg-uvic/image-matching-benchmark>

² <https://vision.uvic.ca/image-matching-challenge>

1 Introduction

Matching two or more views of a given scene is at the core of fundamental computer vision problems, including image retrieval [55, 9, 78, 104, 71], 3D reconstruction [3, 48, 90, 121], re-localization [85, 86, 58], and SLAM [69, 33, 35]. Despite decades of research, image matching remains unsolved in the general, wide-baseline scenario. It is a challenging problem with many factors that need to be taken into account, e.g., viewpoint, illumination, occlusions, and camera properties. Because of this, image matching has traditionally been approached with sparse methods – that is, with local features.

Recent efforts have moved towards *holistic*, end-to-end solutions [51, 12, 25], but despite their promise, they are yet to outperform the *separatists* [88, 120] that are based on the classical paradigm of step-by-step solutions. For example, in a classical wide baseline stereo pipeline [75] we (1) extract local features, such as SIFT [55], (2) build a list of tentative matches by nearest-neighbor search in descriptor space, and (3) retrieve the pose with a minimal solver inside a robust estimator, such as the 7-point algorithm [46] in a RANSAC loop [41]. To build a 3D reconstruction out of a set of images, we feed the same matches to a bundle adjustment pipeline [45, 106] to jointly optimize the camera intrinsics, extrinsics, and 3D point locations. This modular structure simplifies the problem and allows for incremental improvements, of which there have been hundreds, if not thousands.

New methods for each of these sub-problems, such as feature extraction or pose estimation, are typically studied in isolation, using intermediate metrics, which simplifies their evaluation. However, there is no guarantee that gains in one part of the pipeline will translate to the final application, as these components interact in complex ways. For example, patch descriptors, including very recent works [47, 110, 103, 68], are often evaluated on Brown’s seminal patch retrieval database [23], introduced in 2007. They show dramatic improvements – up to 39x relative [110] – over handcrafted methods such as SIFT, but it is unclear whether this remains true on real-world applications. In fact, we later demonstrate that the gap narrows dramatically when decades-old baselines are properly tuned.

We posit that it is time to look beyond intermediate metrics and focus on downstream performance. This is particularly crucial *now*, with deep networks seemingly outperforming algorithmic solutions on classical, sparse problems such as outlier filtering [113, 79, 116, 97, 21], bundle adjustment [99, 93], SfM [109, 7] and SLAM [100, 52]. To this end, we introduce a benchmark for wide-baseline image matching, including:

- (a) A dataset with thousands of phototourism images of 25 landmarks, taken from heterogeneous viewpoints, with different cameras, in varying illumination and weather

conditions – all of which are necessary for a comprehensive evaluation. We reconstruct the scenes with SfM, without the need for human intervention, providing depth maps and ground truth poses for 26k images, and reserve another 4k for a private test set.

- (b) A modular pipeline incorporating dozens of methods for feature extraction, matching, and pose estimation, both classical and state-of-the-art, as well as multiple heuristics, all of which can be swapped out and tuned separately.
- (c) Two downstream tasks – stereo and multi-view reconstruction – evaluated with both downstream and intermediate metrics, for comparison.
- (d) A thorough study of dozens of methods and techniques, both hand-crafted and learned, and their combination, along with a recommended procedure for effective hyper-parameter selection.

This framework enables researchers to evaluate how a new approach performs in a standardized pipeline, both *against* its competitors, and *alongside* state-of-the-art solutions for other components, from which it simply cannot be detached. This is crucial, as true performance can be easily hidden by sub-optimal hyperparameters.

2 Related Work

The literature on image matching is too vast for a thorough overview. We cover relevant methods for feature extraction and matching, pose estimation, 3D reconstruction, applicable datasets, and evaluation frameworks.

2.1 Local features

Local features became a staple in computer vision with the introduction of SIFT [55]. They typically involve three distinct steps: keypoint detection, orientation estimation, and descriptor extraction. Other popular classical solutions are SURF [17], ORB [83], and AKAZE [5].

Modern descriptors often train deep networks on pre-cropped patches, typically from SIFT keypoints (*i.e.* Difference of Gaussians or DoG). They include DeepDesc [94], TFeat [13], L2-Net [102], HardNet [64], SOS-Net [103], and LogPolarDesc [39] – most of them are trained on the same dataset [23]. Recent works leverage additional cues, such as geometry or global context, including GeoDesc [57] and ContextDesc [56]. There have been multiple attempts to learn keypoint detectors separately from the descriptor, including TILDE [108], TCDet [118], QuadNet [89], and Key.Net [15]. An alternative is to treat this as an end-to-end learning problem, a trend that started with the introduction of LIFT [112] and also includes DELF [71], SuperPoint [35], LF-Net [72], D2-Net [38] and R2D2 [81].

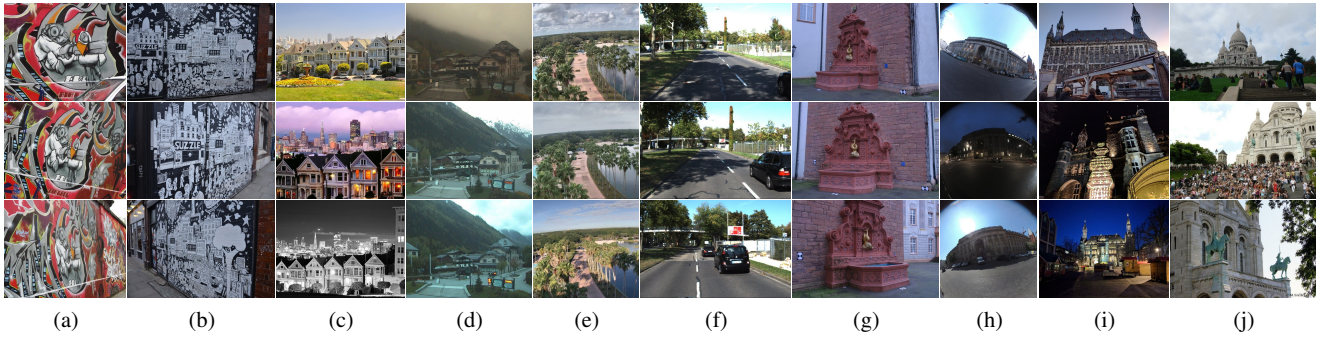


Fig. 2 On the limitations of previous datasets. In order to highlight the need for a new benchmark, we show some examples from datasets and benchmarks featuring posed images that have been previously used to evaluate local features and robust matchers (some images are cropped for the sake of presentation). From left to right: (a) VGG Oxford [61], (b) HPatches [11], (c) Edge Foci [122], (d) Webcam [108], (e) AMOS [49], (f) KITTI [43], (g) Strecha [95], (h) SILDA [40], (i) Aachen [85], (j) Ours. Notice that many of these (a-e) contain only planar structures or illumination changes, which makes it easy – or trivial – to obtain ground truth poses, encoded as homographies. Other datasets are small – (g) contains very accurate depth maps, but only two scenes and 19 images total – or do not contain enough photometric and viewpoint transformations. Aachen (i) is closer to ours (j), but relatively small, limited to one scene, and focused on re-localization on the day vs. night use-case.

2.2 Robust matching

Inlier ratios in wide-baseline stereo can be below 10% – and sometimes even lower. This is typically approached with iterative sampling schemes based on RANSAC [41], relying on closed-form solutions for pose solving such as the 5- [70], 7- [46] or 8-point algorithm [44]. Improvements to this classical framework include local optimization [27], using likelihood instead of reprojection (MLE-SAC) [105], speed-ups using probabilistic sampling of hypotheses (PROSAC) [26], degeneracy check using homographies (DEGENSAC) [29], Graph Cut as a local optimization (GC-RANSAC) [14], and auto-tuning of thresholds using confidence margins (MAGSAC) [32].

As an alternative direction, recent works, starting with CNe (Context Networks) in [113], train deep networks for outlier rejection taking correspondences as input, often followed by a RANSAC loop. Follow-ups include [79, 119, 97, 116]. Differently from RANSAC solutions, they typically process all correspondences in a single forward pass, without the need to iteratively sample hypotheses. Despite their promise, it remains unclear how well they perform in real-world settings, compared to a well-tuned RANSAC.

2.3 Structure from Motion (SfM)

In SfM, one jointly optimizes the location of the 3D points and the camera intrinsics and extrinsics. Many improvements have been proposed over the years [3, 48, 30, 42, 121]. The most popular frameworks are VisualSfM [111] and COLMAP [90] – we rely on the latter, to both generate the ground truth and as the backbone of our multi-view task.

2.4 Datasets and benchmarks

Early works on local features and robust matchers typically relied on the Oxford dataset [61], which contains 48 images and ground truth homographies. It helped establish two common metrics for evaluating local feature performance: repeatability and matching score. Repeatability evaluates the keypoint detector: given two sets of keypoints over two images, projected into each other, it is defined as the ratio of keypoints whose support regions’ overlap is above a threshold. The matching score (MS) is similarly defined, but also requires their descriptors to be nearest neighbours. Both require pixel-to-pixel correspondences – *i.e.*, features outside valid areas are ignored.

A modern alternative to Oxford is HPatches [11], which contains 696 images with differences in illumination *or* viewpoint – but not both. However, the scenes are planar, without occlusions, limiting its applicability.

Other datasets that have been used to evaluate local features include DTU [1], Edge Foci [122], Webcam [108], AMOS [76], and Strecha’s [95]. They all have limitations – be it narrow baselines, noisy ground truth, or a small number of images. In fact, most learned descriptors have been trained and evaluated on [24], which provides a database of pre-cropped patches with correspondence labels, and measures performance in terms of patch retrieval. While this seminal dataset and evaluation methodology helped developed many new methods, it is not clear how results translate to different scenarios – particularly since new methods outperform classical ones such as SIFT by orders of magnitude, which suggests overfitting.

Datasets used for navigation, re-localization, or SLAM, in outdoor environments are also relevant to our problem. These include KITTI [43], Aachen [87], Robotcar [59], and CMU seasons [86, 10]. However, they do not feature the wide range of transformations present in phototourism data.



Fig. 3 Phototourism dataset. Some images from our dataset and their corresponding depth maps, with occluded pixels shown in red.

Megadepth [54] is a more representative, phototourism-based dataset, which using COLMAP, as in our case – it could, in fact, easily be folded into ours.

Modern benchmarks, by contrast, are few and far between – they include VLBenchmark [50], HPatches [11], and SILDA [40] – all limited in scope. A large-scale benchmark for SfM was proposed in [91], which built 3D reconstructions with different local features. However, only a few scenes contain ground truth, so most of their metrics are qualitative – *e.g.* number of observations or average reprojection error. Yi *et al.* [113] and Bian *et al.* [20] evaluates different methods for pose estimation on several datasets – however, few methods are considered and they are not carefully tuned.

We highlight some of these datasets/benchmarks, and their limitations, in Fig. 2. We are, to the best of our knowledge, the first to introduce a public, modular benchmark for 3D reconstruction with sparse methods using downstream metrics, and featuring a comprehensive dataset with a large range of image transformations.

3 The Phototourism Dataset

While it is possible to obtain very accurate poses and depth maps under controlled scenarios with devices such as LIDAR, this is costly and requires a specific set-up that does not scale well. For example, Strecha’s dataset [95] fits this description but contains only 19 images. We argue that a truly representative dataset must contain a wider range of transformations – including different imaging devices, time of day, weather, partial occlusions, etc. Phototourism images satisfy this condition and are readily available.

We thus build on 25 collections of popular landmarks originally selected in [48, 101], each with hundreds to thousands of images. We downsample them with bilinear interpolation to a maximum size of 1024 pixels along the long-side and pose them with COLMAP [90], which provides us with the (pseudo) ground truth. We do exhaustive image matching before Bundle Adjustment – unlike [92], which uses only 100 pairs for each image – and thus provide enough matching images for any conventional SfM to return near-perfect results under normal circumstances.

The basic principle behind our approach is to obtain a ground truth signal using reliable, off-the-shelf technologies, while making the problem as easy as possible – and then evaluate new technologies on a much harder problem, using only a subset of that data. For example, we reconstruct a scene with hundreds or thousands of images with vanilla COLMAP and then evaluate “modern” features and matchers against its poses using only two images (“stereo”) or up to 25 at a time (“multiview” with SfM). For a discussion regarding the accuracy of our ground truth data, please refer to Section 3.3.

In addition to point clouds, COLMAP provides dense depth estimates. These are noisy, and have no notion of occlusions – *i.e.* a depth value is provided for every pixel. We remove occluded pixels from them using the reconstructed model from COLMAP; see Fig. 3 for examples. We rely on these “cleaned” depth maps to compute classical, pixel-wise metrics – repeatability and matching score. We find that some images are flipped 90°, and use the reconstructed pose to rotate them – along with their poses – so they are roughly ‘upright’, which is a reasonable assumption for this type of data.

3.1 Dataset details

Out of the 25 scenes that contain almost 30k registered images in total, we select 2 for validation and 9 for testing. The rest of the scenes can be used for training – we do not use them in this paper. We provide images, 3D reconstructions, camera poses, and depth maps for every training and validation scene. For the test scenes we release only a subset of 100 images and keep the ground truth private for our challenge – results on this private set can be obtained by sending challenge submissions, which are processed on our side.

We list the scenes used for training and validation in Table 1, and the test scenes in Table 2, along with the acronyms used in several figures. For validation experiments – Sections 5 and 7 – we choose two of the larger scenes, “Sacre Coeur” and “St. Peters Square”, which in our experience provide results that are quite representative of what should be expected on phototourism datasets. These two subsets have been released, so that the validation results are repro-

Name	Images	3D points
“Brandenburg Gate”	1363	100040
“Buckingham Palace”	1676	234052
“Colosseum Exterior”	2063	259807
“Grand Place Brussels”	1083	229788
“Hagia Sophia Interior”	888	235541
“Notre Dame Front Facade”	3765	488895
“Palace of Westminster”	983	115868
“Pantheon Exterior”	1401	166923
“Prague Old Town Square”	2316	558600
“Reichstag”	75	17823
“Sacre Coeur” (SC)	1179	140659
“St. Peter’s Square” (SPS)	2504	232329
“Taj Mahal”	1312	94121
“Temple Nara Japan”	904	92131
“Trevi Fountain”	3191	580673
“Westminster Abbey”	1061	198222
Total	25.7k	3.6M

Table 1 Dataset details: Training and validation.

Name	Images	3D points
“British Museum” (BM)	660	73569
“Florence Cathedral Side” (FCS)	108	44143
“Lincoln Memorial Statue” (LMS)	850	58661
“London (Tower) Bridge” (LB)	629	72235
“Milan Cathedral” (MC)	124	33905
“Mount Rushmore” (MR)	138	45350
“Piazza San Marco” (PSM)	249	95895
“Sagrada Familia” (SF)	401	120723
“St. Paul’s Cathedral” (SPC)	615	98872
Total	3774	643k

Table 2 Dataset details: Test.

ducible and comparable. They can all be downloaded from the challenge website².

3.2 Estimating the co-visibility between two images

When evaluating image pairs, we need to be sure that two given images share a common view – they may be registered by the SfM reconstruction without having any pixels in common, as long as other images can act as a ‘bridge’ between them. For the stereo task, we determine co-visible pairs of images with a simple heuristic. We extract, for each image, the 2D keypoints present in the 3D model, obtain their bounding box, and compute the ratio between its area and the whole image; see Fig. 5 for examples. Given a pair of images, we pick the minimum of the two as the “co-visibility” ratio $v_{i,j} \in [0, 1]$. This co-visibility varies significantly from scene to scene. We histogram it in Fig. 4, providing insights into how “hard” each scene is – without accounting for large occlusions.

For stereo, we set the minimum co-visibility threshold to 0.1. For the multi-view task, we simply select image subsets

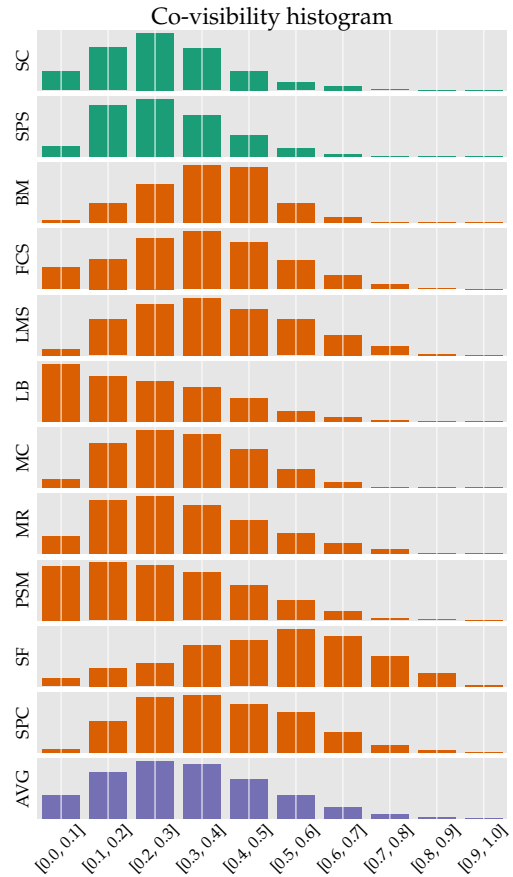


Fig. 4 Co-visibility histogram. We break down the co-visibility measure for each scene in the validation (green) and test (red) sets, as well as the average (purple). Notice how the statistics may vary significantly from scene to scene.

which have at least 100 3D points in common, as in [113, 116]. We find both criteria work well in practice.

3.3 On the quality of our “ground-truth”

Our core assumption is that we can obtain accurate poses from large sets of images without human intervention, which can be used as “ground truth” to evaluate image matching performance on pairs or small subsets of images – a harder, proxy task. Should this assumption hold, the poses retrieved with a large enough number of images would not change as more images are added, and these poses would be the same regardless of which local feature is used.

To validate this, we pick the scene “Sacre Coeur” and compute SfM reconstructions with a varying number of images: 100, 200, 400, 800, and 1179 images (the entire “Sacre Coeur” dataset), where each set contains the previous one, so that new images are being added. These reconstructions are only defined up to scale, and we do not have an absolute scale that can be used to compare them against each other, so we use a simple, pairwise metric instead: we pick any com-

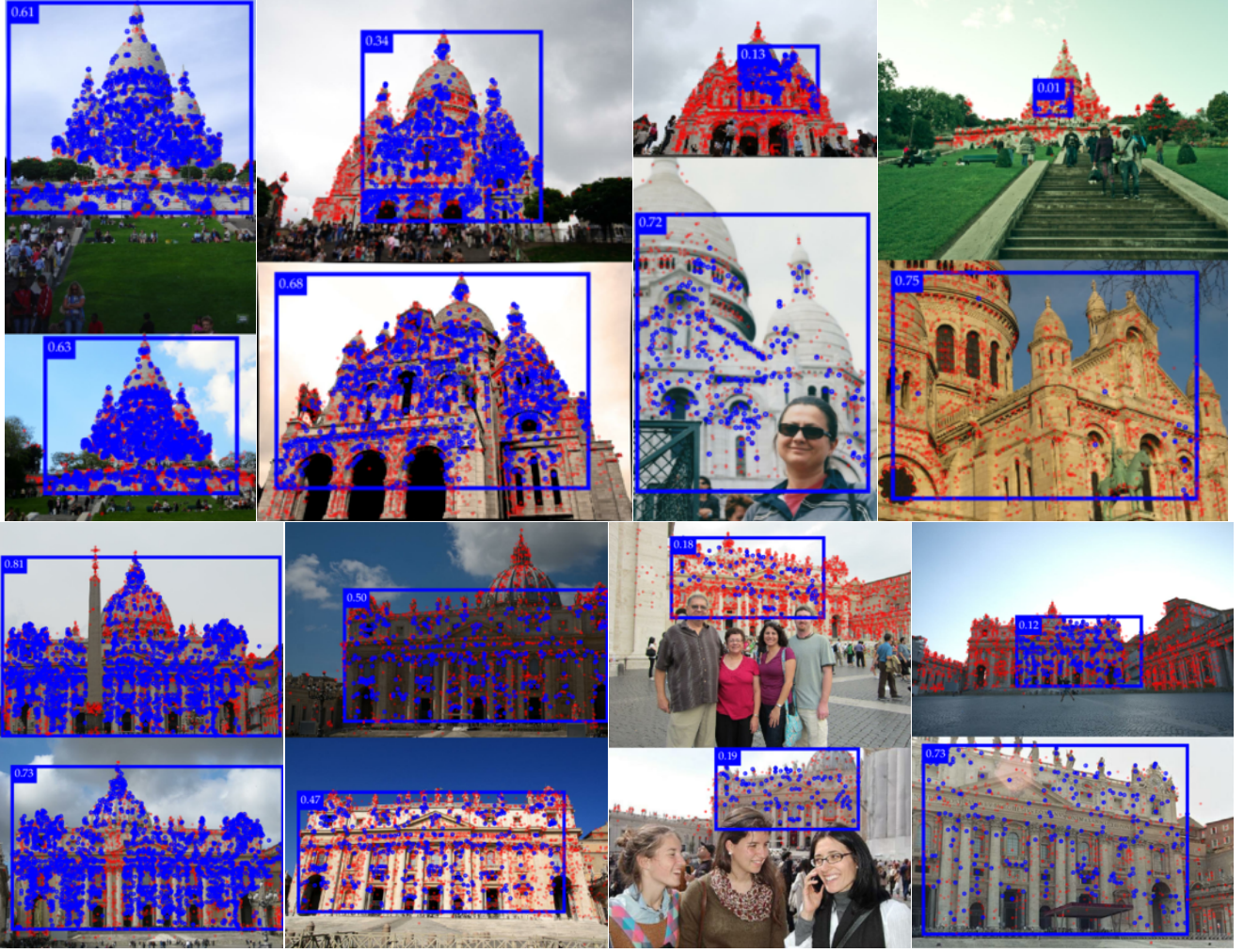


Fig. 5 Co-visibility examples. We show examples of co-visibility values for image pairs from our validation scenes: “Sacre Coeur” (top) and “St. Peter’s Square” (bottom). We plot the image keypoints that survive the 3D reconstruction, in blue if they are co-visible across both images and in red otherwise, and the bounding box of the co-visible points, which we use to compute a per-image visibility ratio, shown in the figure. The co-visibility value for the image pair is the lower of these two values. We show examples at different ‘difficulty’ levels. All of these pairs are used in our evaluation except the top-right example, as we set a cut-off at 0.1.

Feature used	Number of images			
	100 vs. all	200 vs. all	400 vs. all	800 vs. all
SIFT [55]	0.46° / 0.13°	0.42° / 0.11°	0.32° / 0.08°	0.39° / 0.08°
SuperPoint [34]	2.09° / 1.57°	2.09° / 1.54°	1.87° / 1.21°	2.53° / 0.53°
R2D2 [80]	0.41° / 0.14°	0.29° / 0.09°	0.28° / 0.09°	0.21° / 0.06°

Table 3 Pose convergence in SfM. We report the mean/median of the difference (in degrees) between the poses extracted with the full set of 1179 images for “Sacre Coeur”, and different subsets of it, for three local feature methods – to keep the results comparable we only look at the 100 images in common across all subsets. We report the maximum among the angular difference between rotation matrices and translation vectors. The estimated poses are stable, with as low as 100 images.

bination of two out of the 100 images present in the smallest subset, and compare how much they change with respect to their counterparts reconstructed using the entire set – we do this for every subset, *i.e.*, 100, 200, etc. Ideally, we would

Reference	Compared	
	SuperPoint [34]	R2D2 [80]
SIFT [55]	2.06° / 1.57°	0.42° / 0.14°

Table 4 Difference between poses obtained with different local features. We report the mean/median of the difference (in degrees) between the poses extracted with SuperPoint or R2D2, and those extracted with SIFT. We use the maximum of the angular error between rotation matrices and translation vectors. They are very similar – R2D2 and SIFT give near-identical results.

like the differences between the poses to approach zero as more images are added. We list the results in Table 3, for different local feature methods. Notice how the poses converge, especially in terms of median, as more images are used, for all methods – and that the reconstructions using only 100 images are already very stable. For SuperPoint we

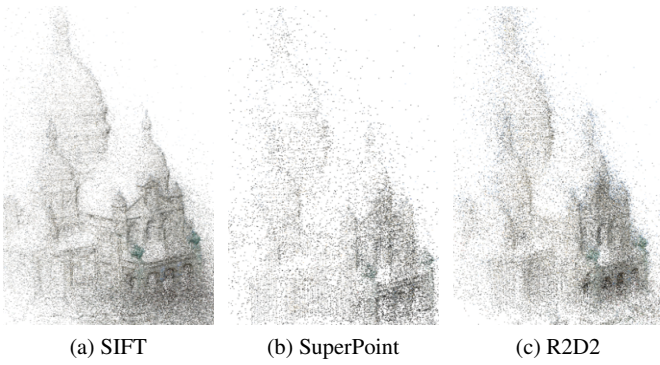


Fig. 6 COLMAP with different local features. We show the reconstructed point cloud for the scene “Sacre Coeur” using three different local features: SIFT, SuperPoint, and R2D2, using all the images available (1179). The reconstructions with SIFT and R2D2 are both dense, albeit somewhat different. The reconstruction with SuperPoint is quite dense, considering it can only extract a much smaller number of features effectively, but its poses appear less accurate.

use a smaller number of features (2k per image), which is not enough to achieve pose convergence, but the error is still reduced as more images are used.

We conduct a second experiment to verify that there is no bias towards using SIFT features for obtaining the ground truth. We compare the poses obtained with SIFT to those obtained with other local features – note that our primary metric uses nothing but the *estimated poses* for evaluation. We report these results in Table 4. The pose differences between SIFT and SuperPoint or R2D2 are not large. In fact, given that SuperPoint is still showing pose changes amongst itself on Table 3, at about the same magnitude as those reported here, we conjecture that the reconstructions with SuperPoint which cannot extract a large number of keypoints are less accurate. This is further supported by the fact that the point cloud obtained with the entire scene generated with SuperPoint is less dense (125K 3D points) than the ones generated with SIFT (438K) or R2D2 (317k); see Fig. 6. Note also that the poses from R2D2 are nearly identical to those from SIFT.

These observations reinforce our trust on the accuracy of our ground truth – given sufficient images, the choice of local feature is irrelevant, at least for the purpose of retrieving accurate poses. Our evaluation considers pose errors of up to 10° , at a resolution of 1° – significantly smaller than the fluctuations observed here, which we consider negligible. Note that these conclusions may not hold on large-scale SfM requiring loop closures, but our dataset contains landmarks, which do not suffer from this problem.

In addition, we note that the use of dense, ground truth depth from SfM, which is arguably less accurate, has been verified by multiple parties, for training and evaluation, including: CNe [113], DFE [79], LF-Net [72], D2-Net [38], LogPolarDesc [39], OANet [117], and Super-

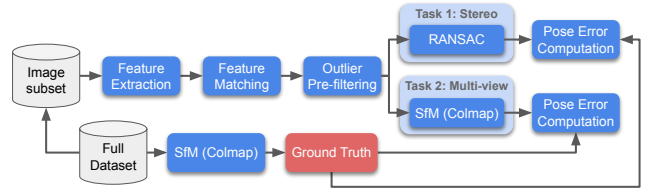


Fig. 7 Our benchmark pipeline. It takes a subset of N images of a scene as input, extracts features for each, and computes matches for all M image pairs, $M = \frac{1}{2}N(N-1)$. After an optional filtering step, the matches are fed to two different tasks. Performance is measured *downstream*, by a pose-based metric, common across tasks. The ground truth is extracted once, on the full set of images.

Glue [84] among others, suggesting it is sufficiently accurate – several of these rely on the data used in our paper.

As a final observation, while the poses are *stable*, they could still be *incorrect*. This can happen on extremely symmetric structures: for instance, a tower with a square or circular cross section. In order to prevent such errors from creeping into our evaluation, we visually inspected all the images in our test set. Out of 900 of them, we found 4 mis-registered samples, all of them from the same scene, “London Bridge”, which were removed from our data.

4 Pipeline

We outline our pipeline in Fig. 7. It takes as input $N=100$ images per scene. The feature extraction module computes up to K features from each image. The feature matching module generates a list of putative matches for each image pair, *i.e.* $\frac{1}{2}N(N-1) = 4950$ combinations. These matches can be optionally processed by an outlier pre-filtering module. They are then fed to two tasks: stereo, and multiview reconstruction with SfM. We now describe each of these components in detail.

4.1 Feature extraction

We consider three broad families of local features. The first includes full, “classical” pipelines, most of them hand-crafted: SIFT [55] (and RootSIFT [8]), SURF [17], ORB [83], and AKAZE [5]. We also consider FREAK [4] descriptors with BRISK [53] keypoints. We take these from OpenCV. For all of them, except ORB, we lower the detection threshold to extract more features, which increases performance when operating with a large feature budget. We also consider DoG alternatives from VLFeat [107]: (VL-)DoG, Hessian [18], Hessian-Laplace [62], Harris-Laplace [62], MSER [60]; and their affine-covariant versions: DoG-Affine, Hessian-Affine [62, 16], DoG-AffNet [66], and Hessian-AffNet [66].

The second group includes descriptors learned on DoG keypoints: L2-Net [102], Hardnet [64], Geodesc [57], SOS-Net [103], ContextDesc [56], and LogPolarDesc [39].

The last group consists of pipelines learned end-to-end (e2e): Superpoint [35], LF-Net [72], D2-Net [38] (with both single- (SS) and multi-scale (MS) variants), and R2D2 [80].

Additionally, we consider Key.Net [15], a learned detector paired with HardNet descriptors – we pair it with original implementation of HardNet instead than the one provided by the authors, as it performs better³.

4.2 Feature matching

We break this step into four stages. Given images \mathbf{I}^i and \mathbf{I}^j , $i \neq j$, we create an initial set of matches by nearest neighbor (NN) matching from \mathbf{I}^i to \mathbf{I}^j , obtaining a set of matches $\mathbf{m}_{i \rightarrow j}$. We optionally do the same in the opposite direction, $\mathbf{m}_{j \rightarrow i}$. We then apply Lowe’s ratio test [55] to each list to filter out non-discriminative matches, with a threshold $r \in [0, 1]$, creating “curated” lists $\tilde{\mathbf{m}}_{i \rightarrow j}$ and $\tilde{\mathbf{m}}_{j \rightarrow i}$. We obtain the final set of putative matches by taking their intersection, $\tilde{\mathbf{m}}_{i \rightarrow j} \cap \tilde{\mathbf{m}}_{j \rightarrow i} = \tilde{\mathbf{m}}_{i \leftrightarrow j}^\cap$ (known in the literature as one-to-one, mutual NN, bipartite, or cycle-consistent), or their union $\tilde{\mathbf{m}}_{i \rightarrow j} \cup \tilde{\mathbf{m}}_{j \rightarrow i} = \tilde{\mathbf{m}}_{i \leftrightarrow j}^\cup$ (symmetric). We refer to them as “both” and “either”, respectively. We also implement a simple unidirectional matching, *i.e.*, $\tilde{\mathbf{m}}_{i \rightarrow j}$. Finally, we optionally apply a distance filter, removing matches whose distance is above a threshold.

The “both” strategy is similar to the “symmetrical nearest neighbor ratio” (sNNR) [19], proposed concurrently – sNNR combines the nearest neighbor ratio in both directions into a single number by taking the harmonic mean, while our test takes the maximum of the two values.

4.3 Outlier pre-filtering

Context Networks [113], or CNe for short, proposed a method to find sparse correspondences with a permutation-equivariant deep network based on PointNet [77], sparking a number of follow-up works [79, 31, 119, 116, 97]. We embed CNe into our framework. It often works best when paired with RANSAC [113, 97], so we consider it as an *optional* pre-filtering step before it – and apply it to both stereo and multiview. As the published model was trained on one of our validation scenes, we re-train it on “Notre Dame Front Facade” and “Buckingham Palace”, following their training protocol, *i.e.*, with 2000 SIFT features, unidirectional matching, and no ratio test. We evaluated the new model on the test set and observed that its performance is better than

³ In [15] the models are converted to TensorFlow – we use the original PyTorch version.

the one that was released by the authors. It could be further improved by using different matching schemes, such as bidirectional matching, but we have not explored this in this paper and leave as future work.

We perform one additional, but necessary, change: CNe (like most of its successors) was originally trained to estimate the Essential matrix instead of the Fundamental matrix [113], *i.e.*, it assumes known intrinsics. In order to use it within our setup, we simply normalize the coordinates by the size of the image instead of using ground truth calibration matrices. This strategy has also been used in [97], and has been shown to work well in practice.

4.4 Stereo task

The list of tentative matches is given to a robust estimator, which we use to estimate $\mathbf{F}_{i,j}$, the Fundamental matrix between \mathbf{I}_i and \mathbf{I}_j . In addition to (locally-optimized) RANSAC [41, 28], as implemented in OpenCV [22], and sklearn [73], we consider more recent algorithms with publicly available implementations: DEGENSAC [29], GC-RANSAC [14] and MAGSAC [32]. For DEGENSAC we additionally consider disabling the degeneracy check, which theoretically should be equivalent to the OpenCV and sklearn implementations – we call this variant “PyRANSAC”. Given $\mathbf{F}_{i,j}$, we use the known intrinsics $\mathbf{K}_{\{i,j\}}$ to compute the Essential matrix $\mathbf{E}_{i,j}$, as $\mathbf{E}_{i,j} = \mathbf{K}_j^T \mathbf{F}_{i,j} \mathbf{K}_i$. Finally, we recover the relative rotation and translation vectors with a cheirality check with OpenCV’s `recoverPose`.

4.5 multiview task

Large-scale SfM is notoriously hard to evaluate, as it requires accurate ground truth. Since our goal is to benchmark *local features* and *matching methods*, and not SfM algorithms, we opt for a different strategy. We reconstruct a scene from small image subsets, which we call “bags”. We consider bags of 5, 10, and 25 images, which are randomly sampled from the original set of 100 images per scene – with a co-visibility check. We create 100 bags for bag sizes 5, 50 for bag size 10, and 25 for bag size 25 – *i.e.*, 175 SfM runs in total.

We use COLMAP [90], feeding it the matches computed by the previous module – note that this comes before the robust estimation step, as COLMAP implements its own RANSAC. If multiple reconstructions are obtained, we consider the largest one. We also collect and report statistics such as the number of landmarks or the average track length. Both statistics and error metrics are averaged over the three bag sizes, each of which is in turn averaged over its individual bags.

4.6 Error metrics

Since the stereo problem is defined up to a scale factor [45], our main error metric is based on *angular errors*. We compute the difference, in degrees, between the *estimated* and *ground-truth* translation and rotation *vectors* between two cameras. We then threshold it over a given value for all possible – *i.e.*, co-visible – pairs of images. Doing so over different angular thresholds renders a curve. We compute the mean Average Accuracy (mAA) by integrating this curve up to a maximum threshold, which we set to 10° – this is necessary because large errors always indicate a bad pose: 30° is not necessarily better than 180° , both estimates are wrong. Note that by computing the area under the curve we are giving more weight to methods which are more accurate at lower error thresholds, compared to using a single value at a certain designated threshold.

This metric was originally introduced in [113], where it was called mean Average Precision (mAP). We argue that “accuracy” is the correct terminology, since we are simply evaluating how many of the predicted poses are “correct”, as determined by thresholding over a given value – *i.e.*, our problem does not have “false positives”.

We use the same metric for multiview. Since we do not know the scale of the scene *a priori*, it is not possible to measure translation error in metric terms. While we intend to explore this in the future, such a metric, while more interpretable, is not without problems – for instance, the range of the distance between the camera and the scene can vary drastically from scene to scene and make it difficult to compare their results. To compute the mAA in pose estimation for the multiview task, we simply take the mean of the average accuracy for every pair of cameras – setting the pose error to ∞ for pairs containing unregistered views. If COLMAP returns multiple models which cannot be co-registered (which is rare) we consider only the largest of them for simplicity.

For the stereo task, we can report this value for different co-visibility thresholds: we use $v = 0.1$ by default, which preserves most of the “hard” pairs. Note that this is not applicable to the multiview task, as all images are registered at once via bundle adjustment in SfM.

Finally, we consider repeatability and matching score. Since many end-to-end methods do not report and often do not have a clear measure of scale – or support region – we simply threshold by pixel distance, as in [82]. For the multiview task, we also compute the Absolute Trajectory Error (ATE) [96], a metric widely used in SLAM. Since, once again, the reconstructed model is scale-agnostic, we first scale the reconstructed model to that of the ground truth and then compute the ATE. Note that ATE needs a minimum of three points to align the two models.

4.7 Implementation

Our code has been open-sourced¹ along with every method used in the paper⁴. Our implementation relies on SLURM [114] for scalable job scheduling, which is compatible with our supercomputer clusters – we also provide on-the-cloud, ready-to-go images⁵. The benchmark can also run on a standard computer, sequentially. It is computationally expensive, as it requires matching about 45k image pairs. The most costly step – leaving aside feature extraction, which is very method-dependent – is typically feature matching: 2–6 seconds per image pair⁶, depending on descriptor size. Outlier pre-filtering takes about 0.5–0.8 seconds per pair, excluding some overhead to reformat the data into its expected format. RANSAC methods vary between 0.5–1 second – as explained in Section 5 we limit their number of iterations based on a compute budget, but the actual cost depends on the number of matches. Note that these values are computed on the validation set – for the test set experiments we increase the RANSAC budget, in order to remain compatible with rules of our challenge. We find COLMAP to vary drastically between set-ups. New methods will be continuously added, and we welcome contributions to the code base.

5 Details are Important

Our experiments indicate that each method needs to be carefully tuned. In this section we outline the methodology we used to find the right hyperparameters on the validation set, and demonstrate why it is crucial to do so.

5.1 RANSAC: Leveling the field

Robust estimators are, in our experience, the most sensitive part of the stereo pipeline, and thus the one we first turn to. All methods considered in this paper have three parameters in common: the confidence level in their estimates, τ ; the outlier (epipolar) threshold, η ; and the maximum number of iterations, I . We find the confidence value to be the least sensitive, so we set it to $\tau = 0.999999$.

We evaluate each method with different values for I and η , using reasonable defaults: 8k SIFT features with bidirectional matching with the “both” strategy and a ratio test threshold of 0.8. We plot the results in Fig. 8, against their computational cost – for the sake of clarity we only show

⁴ <https://github.com/vcg-uvic/image-matching-benchmark-baselines>

⁵ <https://github.com/etrulls/slurm-gcp>

⁶ All of these values are computed on n1-standard-2 VMs on Google Cloud Compute: 2 vCPUs with 7.5 GB of RAM and no GPU.

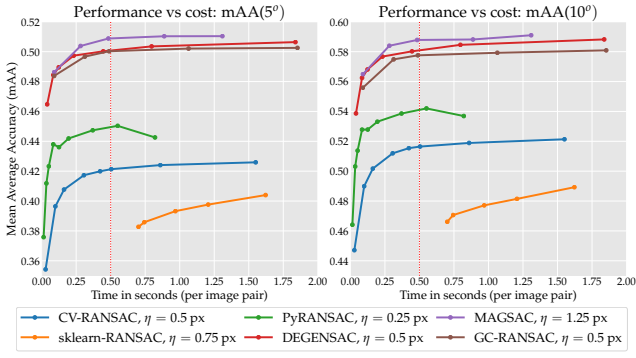


Fig. 8 Validation – Performance vs. cost for RANSAC. We evaluate six RANSAC variants, using 8k SIFT features with “both” matching and a ratio test threshold of $r=0.8$. The inlier threshold η and iterations limit Γ are variables – we plot only the best η for each method, for clarity, and set a budget of 0.5 seconds per image pair (dotted red line). For each RANSAC variant, we pick the largest Γ under this time “limit” and use it for all validation experiments. Computed on ‘n1-standard-2’ VMs on Google Compute (2 vCPUs, 7.5 GB).

the curve corresponding to the best reprojection threshold η for each method.

Our aim with this experiment is to place all methods on an “even ground” by setting a common budget, as we need to find a way to compare them. We pick 0.5 seconds, where all methods have mostly converged. Note that these are different implementations and are obviously not directly comparable to each other, but this is a simple and reasonable approach. We set this budget by choosing Γ as per Fig. 8, instead of actually *enforcing* a time limit, which would not be comparable across different set-ups. Optimal values for Γ can vary drastically, from 10k for MAGSAC to 250k for PyRANSAC. MAGSAC gives the best results for this experiment, closely followed by DEGENSAC. We patch OpenCV to increase the limit of iterations, which was hardcoded to $\Gamma = 1000$; this patch is now integrated into OpenCV. This increases performance by 10-15% relative, within our budget. However, PyRANSAC is significantly better than OpenCV version even with this patch, so we use it as our “vanilla” RANSAC instead. The sklearn implementation is too slow for practical use.

We find that, in general, default settings can be woefully inadequate. For example, OpenCV recommends $\tau = 0.99$ and $\eta = 3$ pixels, which results in a mAA at 10° of 0.3642 on the validation set – a performance drop of 29.3% relative.

5.2 RANSAC: One method at a time

The last free parameter is the inlier threshold η . We expect the optimal value for this parameter to be different for each local feature, with looser thresholds required for methods operating on higher recall/lower precision, and end-to-end methods trained on lower resolutions.

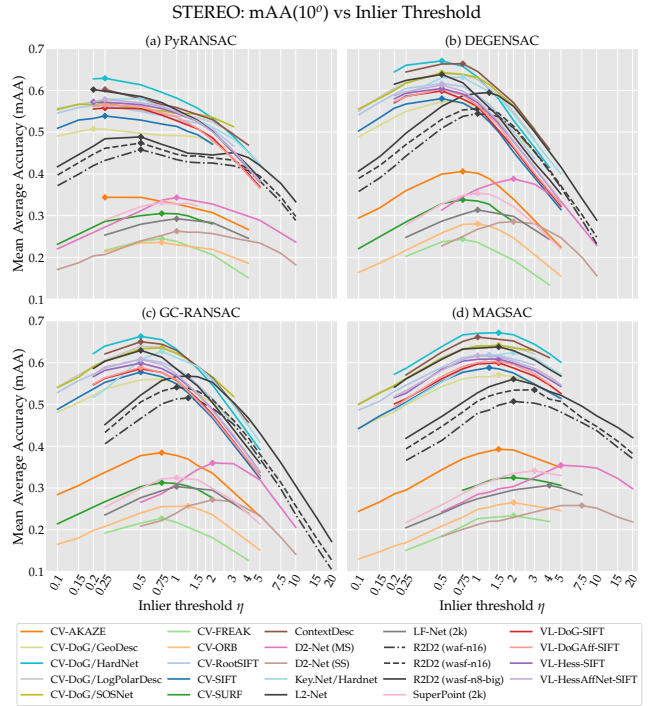


Fig. 9 Validation – Inlier threshold for RANSAC, η . We determine η for each combination, using 8k features (2k for LF-Net and SuperPoint) with the “both” matching strategy and a reasonable value for the ratio test. Optimal parameters (diamonds) are listed in the Section 7.

We report a wide array of experiments in Fig. 9 that confirm our intuition: descriptors learned on DoG keypoints are clustered, while others vary significantly. Optimal values are also different for each RANSAC variant. We use the ratio test with the threshold recommended by the authors of each feature, or a reasonable value if no recommendation exists, and the “both” matching strategy – this cuts down on the number of outliers.

5.3 Ratio test: One feature at a time

Having “frozen” RANSAC, we turn to the feature matcher – note that it comes *before* RANSAC, but it cannot be evaluated in isolation. We select PyRANSAC as a “baseline” RANSAC and evaluate different ratio test thresholds, separately for the stereo and multiview tasks. For this experiment, we use 8k features with all methods, except for those which cannot work on this regime – SuperPoint and LF-Net. This choice will be substantiated in Section 5.4. We report the results for bidirectional matching with the “both” strategy in Fig. 10, and with the “either” strategy in Fig. 11. We find that “both” – the method we have used so far – performs best overall. Bidirectional matching with the “either” strategy produces many (false) matches, increasing the computational cost in the estimator, and requires very small ratio test thresholds – as low as $r=0.65$. Our experiments with

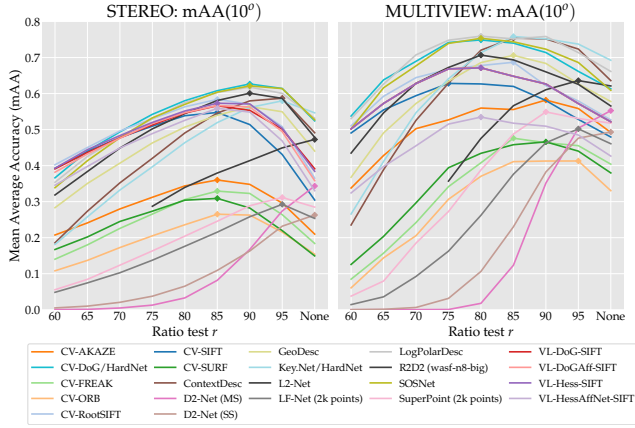


Fig. 10 Validation – Optimal ratio test r for matching with ‘both’. We evaluate bidirectional matching with the ‘both’ strategy (the best one), and different ratio test thresholds r , for each feature type. We use 8k features (2k for SuperPoint and LF-Net). For stereo, we use PyRANSAC.

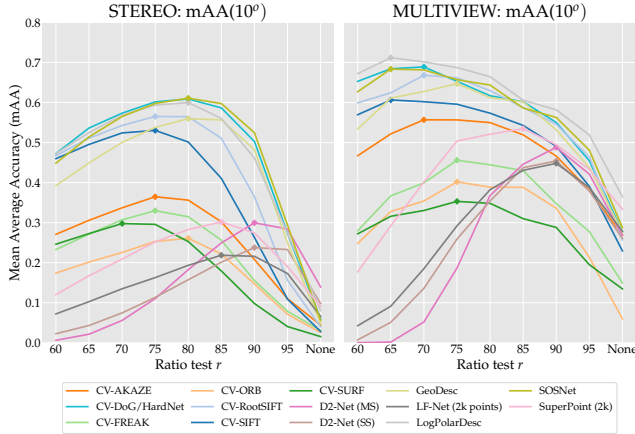


Fig. 11 Validation – Optimal ratio test r for matching with ‘either’. Equivalent to Fig. 10 but with the ‘either’ matching strategy. This strategy requires aggressive filtering and does not reach the performance of ‘both’, we thus explore only a subset of the methods.

unidirectional matching indicate that is slightly worse, and it depends on the order of the images, so we did not explore it further.

As expected, each feature requires different settings, as the distribution of their descriptors is different. We also observe that optimal values vary significantly between stereo and multiview, even though one might expect that bundle adjustment should be able to better deal with outliers. We suspect this might be due to potentially sub-optimal parameters on COLMAP’s RANSAC – we will evaluate this in the future.

Note how the ratio test is critical for performance, and one could arbitrarily select a threshold that favours one method over another, which shows the importance of proper benchmarking. Interestingly, D2-Net is the *only* method that clearly performs best without the ratio test. It also performs

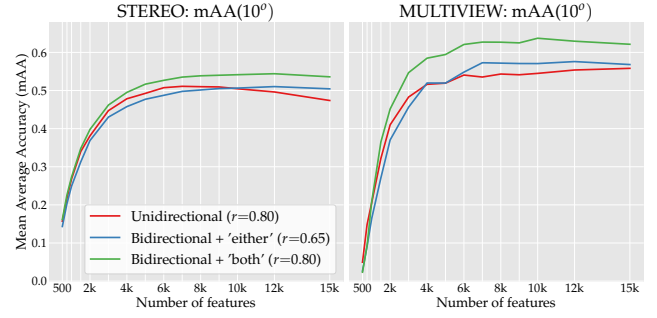


Fig. 12 Validation – Number of features. Performance on the stereo and multi-view tasks while varying the number of SIFT features, with three matching strategies, and reasonable defaults for the ratio test r .

poorly overall in our evaluation, despite reporting state-of-the-art results in other benchmarks [61, 11, 85, 98] – without the ratio test, the number of tentative matches might be too high for RANSAC or COLMAP to perform well.

Additionally, we implement the first-geometric-inconsistent ratio threshold, or FGINN [65]. We find that although it improves over unidirectional matching, its gains mostly disappear against matching with ‘both’. We report these results in Section 7.2.

5.4 Choosing the number of features

The ablation tests in this section use (up to) $K=8000$ feature (2k for SuperPoint and LF-Net, as they are trained to extract fewer keypoints). This number is commensurate with that used by SfM frameworks [111, 90]. We report performance for different values of K in Fig. 12. We use PyRANSAC with reasonable defaults for all three matching strategies, with SIFT features.

As expected, performance is strongly correlated with the number of features. We find 8k to be a good compromise between performance and cost, and also consider 2k (actually 2048) as a ‘cheaper’ alternative – this also provides a fair comparison with some learned methods which only operate on that regime. We choose these two values as valid categories for the open challenge linked to the benchmark, and do the same on this paper for consistency.

5.5 Additional experiments

Some methods require additional considerations before evaluating them on the test set. We briefly discuss them in this section. Further experiments are available in Section 7.

Binary features (Fig. 13). We consider three binary descriptors: ORB [83], AKAZE [5], and FREAK [4]. Binary descriptor papers historically favour a distance threshold in place of the ratio test to reject non-discriminative matches [83], although some papers have used the ratio test for ORB

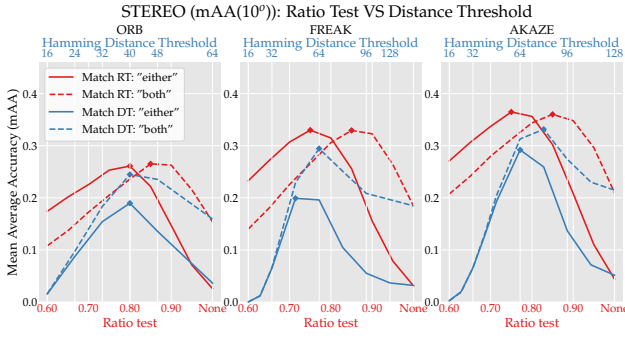


Fig. 13 Validation – Matching binary descriptors. We filter out non-discriminative matches with the ratio test or a distance threshold. The latter (the standard) performs worse in our experiments.

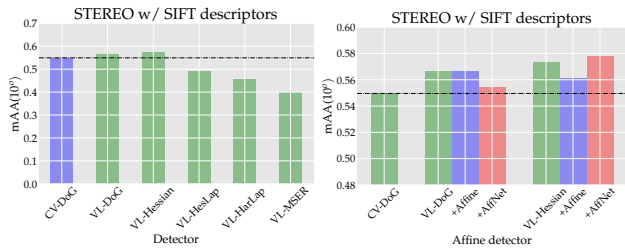


Fig. 14 Validation – Benchmarking detectors. We evaluate the performance on the stereo task while pairing different detectors with SIFT descriptors. The dashed, black line indicates OpenCV SIFT – the baseline. **Left:** OpenCV DoG vs. VLFeat implementations of blob detectors (DoG, Hessian, HesLap) and corner detectors (Harris, HarLap), and MSER. **Right:** Affine shape estimation for DoG and Hessian keypoints, against the plain version. We consider a classical approach, Baumberg (Affine) [16], and the recent, learned AffNet [66] – they provide a small but inconsistent boost.

descriptors [6]. We evaluate both in Fig. 13 – as before, we use up to 8k features and matching with the “both” strategy. The ratio test works better for all three methods – we use it instead of a distance threshold for all experiments in the paper, including those in the previous sections.

On the influence of the detector (Fig. 14). We embed several popular blob and corner detectors into our pipeline, with OpenCV’s DoG [55] as a baseline. We combine multiple methods, taking advantage of the VLFeat library: Difference of Gaussians (DoG), Hessian [18], HessianLaplace [62], HarrisLaplace [62], MSER [60], DoGAffine, Hessian-Affine [62, 16], DoG-AffNet [66], and Hessian-AffNet [66]. We pair them with SIFT descriptors, also computed with VLFeat, as OpenCV cannot process affine keypoints, and report the results in Fig. 14. VLFeat’s DoG performs marginally better than OpenCV’s. Its affine version gives a small boost. Given the small gain and the infrastructure burden of interacting with a Matlab/C library, we use OpenCV’s DoG implementation for most of this paper.

On increasing the support region (Fig. 15). The size (“scale”) of the support region used to compute a descriptor can significantly affect its performance [37, 115, 2]. We

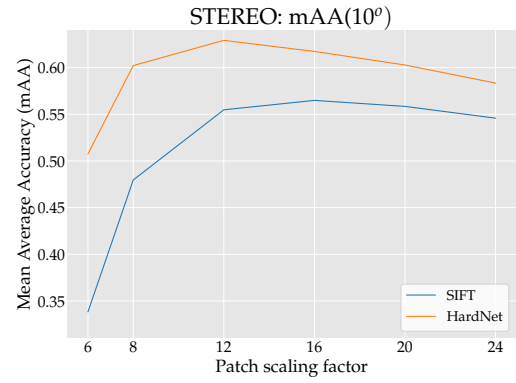


Fig. 15 Validation – Scaling the descriptor support region. Performance with SIFT and HardNet descriptors while applying a scaling factor λ to the keypoint scale (note that OpenCV’s default value is $\lambda=12$). We consider SIFT and HardNet. Default values are optimal or near-optimal.

experiment with different scaling factors, using DoG with SIFT and HardNet [64], and find that $12\times$ the OpenCV scale (the default value) is already nearly optimal, confirming the findings reported in [39]. We show these results in Fig. 15. Interestingly, SIFT descriptors do benefit from increasing the scaling factor from 12 to 16, but the difference is very small – we thus use the recommended value of 12 for the rest of the paper. This, however, suggests that deep descriptors such as HardNet might be able to increase performance slightly by training on larger patches.

6 Establishing the State of the Art

With the findings and the optimal parameters found in Section 5, we move on to the test set, evaluating many methods with their optimal settings. All experiments in this section use bidirectional matching with the “both” strategy. We consider a large feature budget (up to 8k features) and a smaller one (up to 2k), and evaluate many detector/descriptor combinations.

We make three changes with respect to the validation experiments of the previous section. (1) We double the RANSAC budget from 0.5 seconds (used for validation) to 1 second per image pair, and adjust the maximum number of iterations I accordingly – we made this decision to encourage participants to the challenge based on this benchmark to use built-in methods rather than run RANSAC themselves to squeeze out a little extra performance, and use the same values in the paper for consistency. (2) We run each stereo and multiview evaluation three times and average the results, in order to decrease the potential randomness in the results – in general, we found the variations within these three runs to be negligible. (3) We use brute-force to match descriptors instead of FLANN, as we observed a drop in performance. For more details, see Section 6.6 and Table 12.

Method	PyRANSAC			DEGENSAC		MAGSAC		Rank
	NF	NI [†]	mAA(10°) [†]	NI [†]	mAA(10°) [†]	NI [†]	mAA(10°) [†]	
CV-SIFT	7861.1	167.6	.3996	243.6	.4584	297.4	.4583	13
VL-SIFT	7880.6	179.7	.3999	261.6	.4655	326.2	.4633	12
VL-Hessian-SIFT	8000.0	204.4	.3695	290.2	.4450	348.9	.4335	14
VL-DoGAff-SIFT	7892.1	171.6	.3984	250.1	.4680	317.1	.4666	10
VL-HesAffNet-SIFT	8000.0	209.3	.3933	299.0	.4679	350.0	.4626	11
CV-√SIFT	7860.8	192.3	.4228	281.7	.4930	347.5	.4941	9
CV-SURF	7730.0	107.9	.2280	113.6	.2593	145.3	.2552	18
CV-AKAZE	7857.1	131.4	.2570	246.8	.3074	301.8	.3036	16
CV-ORB	7150.2	123.7	.1220	150.0	.1674	178.9	.1570	21
CV-FREAK	8000.0	123.3	.2273	131.0	.2711	196.7	.2656	17
L2-Net	7861.1	213.8	.4621	366.0	.5295	481.0	.5252	5
DoG-HardNet	7861.1	286.5	.4801	432.3	.5543	575.1	.5502	2
DoG-HardNetAmos+	7861.0	265.7	.4607	398.6	.5385	528.7	.5329	3
Key.Net-HardNet	7997.6	448.1	.3997	598.3	.4986	815.4	.4739	8
GeoDesc	7861.1	205.4	.4328	348.5	.5111	453.4	.5056	7
ContextDesc	7859.0	278.2	.4684	493.6	.5098	544.1	.5143	6
SOSNet	7861.1	281.6	.4784	424.6	.5587	563.3	.5517	1
LogPolarDesc	7861.1	254.4	.4574	441.8	.5340	591.2	.5238	4
D2-Net (SS)	5665.3	280.8	.1933	482.3	.2228	781.3	.2032	20
D2-Net (MS)	6924.1	278.2	.2160	470.6	.2506	741.2	.2321	19
R2D2 (wasf-n8-big)	7940.5	457.6	.3683	842.2	.4437	998.9	.4236	15

Table 5 Test – Stereo results with 8k features. We report: (NF) Number of Features; (NI) Number of Inliers produced by RANSAC; and mAA(10°). Top three methods by mAA marked in red, green and blue.

Method	NL [†]	SR [†]	RC [†]	TL [†]	mAA(5°) [†]	mAA(10°) [†]	ATE [‡]	Rank
CV-SIFT	2577.6	96.7	94.1	3.95	.5309	.6261	.4721	13
VL-SIFT	3030.7	97.9	95.4	4.17	.5273	.6283	.4669	12
VL-Hessian-SIFT	3209.1	97.4	94.1	4.13	.4857	.5866	.5175	15
VL-DoGAff-SIFT	3061.5	98.0	96.2	4.11	.5263	.6296	.4751	11
VL-HesAffNet-SIFT	3327.7	97.7	95.2	4.08	.5049	.6069	.4897	14
CV-√SIFT	3312.1	98.5	96.6	4.13	.5778	.6765	.4485	8
CV-SURF	2766.2	94.8	92.6	3.47	.3897	.4846	.6251	17
CV-AKAZE	4475.9	99.0	95.4	3.88	.4516	.5553	.5715	16
CV-ORB	3260.3	97.2	91.1	3.45	.2697	.3509	.7377	21
CV-FREAK	2859.1	92.9	91.7	3.53	.3735	.4653	.6229	19
L2-Net	3424.9	98.6	96.2	4.21	.5661	.6644	.4482	9
DoG-HardNet	4001.4	99.5	97.7	4.34	.6090	.7096	.4187	1
DoG-HardNetAmos+	3550.6	98.8	96.9	4.28	.5879	.6888	.4428	5
Key.Net-HardNet	3366.0	98.9	96.7	4.32	.5391	.6483	.4622	10
GeoDesc	3839.0	99.1	97.2	4.26	.5782	.6803	.4445	7
ContextDesc	3732.5	99.3	97.6	4.22	.6036	.7035	.4228	2
SOSNet	3796.0	99.3	97.4	4.32	.6032	.7021	.4226	3
LogPolarDesc	4054.6	99.0	96.4	4.32	.5928	.6928	.4340	4
D2-Net (SS)	5893.8	99.8	97.5	3.62	.3435	.4598	.6361	20
D2-Net (MS)	6759.3	99.7	98.2	3.39	.3524	.4751	.6283	18
R2D2 (wasf-n8-big)	4432.9	99.7	97.2	4.59	.5775	.6832	.4333	6

Table 6 Test – Multiview results with 8k features. We report: (NL) Number of 3D Landmarks; (SR) Success Rate (%) in the 3D reconstruction across “bags”; (RC) Ratio of Cameras (%) registered in a “bag”; (TL) Track Length or number of observations per landmark; mAA at 5 and 10°; and (ATE) Absolute Trajectory Error. All metrics are averaged across different “bag” sizes, as explained in Section 4. We rank them by mAA at 10° and color-code them as in Table 5.

For stereo, we consider DEGENSAC and MAGSAC, which perform the best in the validation set, and PyRANSAC as a ‘baseline’ RANSAC. We report the results with both 8k features and 2k features in the following subsections. All observations are in terms of mAA, our primary metric, unless stated otherwise.

6.1 Results with 8k features — Tables 5 and 6

On the stereo task, deep descriptors extracted on DoG keypoints are at the top in terms of mAA, with SOSNet being #1, closely followed by HardNet. Interestingly, ‘HardNetAmos+’ [63], a version trained on more datasets – Brown [23],

HPatches [11], and AMOS-patches [63] – performs worse than the original models, trained only on the “Liberty” scene from Brown’s dataset. On the multiview task, HardNet edges out ContextDesc, SOSNet and LogpolarDesc by a small margin.

We also pair HardNet with Key.Net, a learned detector, which performs worse than with DoG when extracting a large number of features – similarly to R2D2, it produces more inliers than DoG but its poses are slightly worse – note that the inliers reported here are the inliers *estimated* by each method, which may still contain outliers.

R2D2, the best performing end-to-end method, does well on multiview (#6), but performs worse than SIFT on stereo – it has a much larger number of inliers than most other methods, which suggests that like D2-Net, its lack of compatibility with the ratio test may be a problem when paired with sample-based robust estimators, due to a lower inlier ratio. D2-net performs poorly on our benchmark, despite state-of-the-art results on others. On the multiview task it creates many more 3D landmarks than any other method. Both issues may be related to its poor localization (pixel) accuracy, due to operating on downsampled feature maps.

Out of the handcrafted methods, SIFT – RootSIFT specifically – remains competitive, being #9 on stereo and #8 on multiview, within 13.1% and 4.9% relative of the top performing method, respectively, while previous benchmarks report differences in performance of *orders of magnitude*. Other “classical” features do not fare so well. One interesting observation is that among these, their ranking on validation and test set is not consistent – Hessian is better on validation than DoG, but significantly worse on the test set, especially in the multiview setup. This further supports the importance of a properly tuned and comprehensive benchmark, such as ours.

Regarding the robust estimators, DEGENSAC and MAGSAC both perform very well, with the former edging out the latter for most local feature methods. This may be due to the nature of the scenes, which often contain dominant planes.

6.2 Results with 2k features — Tables 7 and 8

Results change slightly on the low-budget regime, where Key.Net+HardNet obtains the #1 spot on both tasks. It is closely followed by LogPolarDesc (#2 on stereo and #3 on multiview), a method trained on DoG keypoints – but using a much larger support region, resampled into log-polar patches. R2D2 performs very well on the multiview task (#2), while once again falling a bit short on the stereo task (#7, and 14.5% relative below the #1 method), for which it retrieves a number of inliers significantly larger than its competitors. The rest of the end-to-end methods do not per-

Method	NF	PyRANSAC		DEGENSAC		MAGSAC		Rank
		NI [†]	mAA(10°) [†]	NI [†]	mAA(10°) [†]	NI [†]	mAA(10°) [†]	
CV-SIFT	2048.0	84.9	.2489	79.0	.2875	99.2	.2805	11
CV-√SIFT	2048.0	84.2	.2724	88.3	.3149	106.8	.3125	9
CV-SURF	2048.0	37.9	.1725	72.7	.2086	87.0	.2081	14
CV-AKAZE	2048.0	96.1	.1780	91.0	.2144	115.5	.2127	13
CV-ORB	2031.8	56.3	.0610	63.5	.0819	71.5	.0765	18
CV-FREAK	2048.0	62.5	.1461	65.6	.1761	78.4	.1698	16
L2-Net	1936.3	66.1	.3131	92.4	.3752	114.7	.3691	5
DoG-HardNet	1936.3	111.9	.3508	117.7	.4029	150.5	.4033	4
Key.Net-HardNet	2048.0	134.4	.3272	174.8	.4139	228.4	.3897	1
GeoDesc	1936.3	98.9	.3127	103.9	.3662	129.7	.3640	6
ContextDesc	2048.0	118.8	.2965	124.1	.3510	146.4	.3485	8
SOSNet	1936.3	111.1	.3536	132.1	.3976	149.6	.4092	3
LogPolarDesc	1936.3	118.8	.3569	124.9	.4115	161.0	.4064	2
D2-Net (SS)	2045.6	107.6	.1157	134.8	.1355	259.3	.1317	17
D2-Net (MS)	2038.2	149.3	.1524	188.4	.1813	302.9	.1703	15
LF-Net	2020.3	100.2	.1927	106.5	.2344	141.0	.2226	12
SuperPoint	2048.0	120.1	.2577	126.8	.2964	127.3	.2676	10
R2D2 (wasf-n16)	2048.0	191.0	.2829	215.6	.3614	215.6	.3614	7

Table 7 Test – Stereo results with 2k features. Same as Table 5.

form so well, other than SuperPoint, which obtains competitive results on the multiview task.

The difference between classical and learned methods is more pronounced than with 8k points, with RootSIFT once again at the top, but now within 31.4% relative of the #1 method on stereo, and 23.3% on multiview. This is somewhat to be expected, given that with fewer keypoints, the quality of each individual point matters more.

6.3 2k features vs 8k features — Figs. 16 and 17

We compare the results between the low- and high-budget regimes in Fig. 16, for stereo (with DEGENSAC), and Fig. 17, for multiview. Note how methods can behave quite differently. Those based on DoG significantly benefit from an increased feature budget, whereas those learned end-to-end may require re-training – this is exemplified by the difference in performance between 2k and 8k for Key.Net+Hardnet, specially on multiview, which is very narrow despite quadrupling the budget. Overall, learned detectors – KeyNet, SuperPoint, R2D2, LF-Net – show relatively better results on multiview setup than on stereo. Our hypothesis is that they have good robustness, but low localization precision.

6.4 Outlier pre-filtering with deep networks — Table 9

Next, we study the performance of CNe [113] for outlier rejection, paired with PyRANSAC, DEGENSAC, and MAGSAC. Its training data does not use the ratio test, so we omit it here too – note that because of this, it expects a relatively large number of input matches. We thus evaluate it only for the 8k feature setting, while using the “both” matching strategy.

Our experiments with SIFT, the local feature used to train CNe, are encouraging: CNe aggressively filters out

Method	NL [†]	SR [†]	RC [†]	TL [†]	mAA(5°) [†]	mAA(10°) [†]	ATE [‡]	Rank
CV-SIFT	1081.2	87.6	87.4	3.70	.3718	.4562	.6136	12
CV-√SIFT	1174.7	90.3	89.4	3.82	.4074	.4995	.5589	11
CV-SURF	1186.6	90.2	88.6	3.55	.3335	.4184	.6701	14
CV-AKAZE	1383.9	94.7	90.9	3.74	.3393	.4361	.6422	13
CV-ORB	683.3	74.9	73.0	3.21	.1422	.1914	.8153	18
CV-FREAK	1075.2	87.2	86.3	3.52	.2578	.3297	.7169	16
L2-Net	1253.3	94.7	92.6	3.96	.4369	.5392	.5419	8
DoG-HardNet	1338.2	96.3	93.7	4.03	.4624	.5661	.5093	5
Key.Net-HardNet	1276.3	97.8	95.7	4.49	.5050	.6161	.4902	1
GeoDesc	1133.6	93.6	91.3	4.02	.4246	.5244	.5455	9
ContextDesc	1504.9	95.6	93.3	3.92	.4529	.5568	.5327	6
SOSNet	1317.4	96.0	93.8	4.05	.4739	.5784	.5194	4
LogPolarDesc	1410.2	96.0	93.8	4.05	.4794	.5849	.5090	3
D2-Net (SS)	2357.9	98.9	94.7	3.39	.2875	.3943	.7010	15
D2-Net (MS)	2177.3	98.2	93.4	3.01	.1921	.3007	.7861	17
LF-Net	1385.0	95.6	90.4	4.14	.4156	.5141	.5738	10
SuperPoint	1184.3	95.6	92.4	4.34	.4423	.5464	.5457	7
R2D2 (wasf-n16)	1228.4	99.4	96.2	4.29	.5045	.6149	.4956	2

Table 8 Test – Multiview results with 2k features. Same as Table 6.

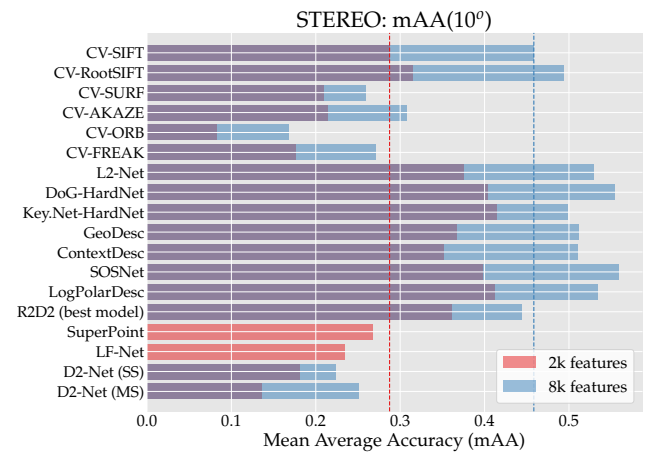


Fig. 16 Test – Stereo performance: 2k vs 8k features. We compare the results obtained with different methods using either 2k or 8k features – we use DEGENSAC, which performs better than other RANSAC variants under most circumstances. Dashed lines indicate SIFT’s performance. For LF-Net and SuperPoint we do not include results with 8k features, as we failed to obtain meaningful results. For R2D2, we use the best model for each setting.

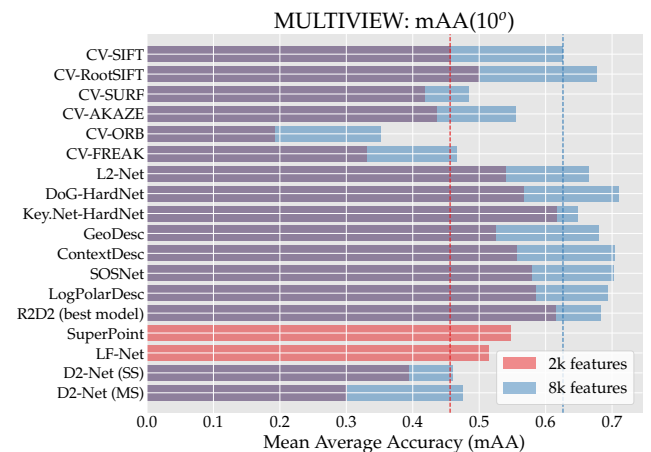


Fig. 17 Test – Multiview performance: 2k vs 8k features. Same as Fig. 16, for multiview.

Method	PyRANSAC		Stereo Task DEGENSAC		MAGSAC		Multi-view Task	
	mAA(10°)↑	Δ(%)↑	mAA(10°)↑	Δ(%)↑	mAA(10°)↑	Δ(%)↑	mAA(10°)↑	Δ(%)↑
CV-SIFT	.4086	+2.24	.4751	+3.65	.4694	+2.42	.6815	+8.85
CV-√SIFT	.4205	-0.53	.4927	-0.06	.4848	-1.87	.6978	+3.16
CV-SURF	.2490	+9.18	.3071	+18.42	.2954	+15.75	.5750	+18.67
CV-AKAZE	.2857	+11.18	.3417	+11.18	.3316	+9.23	.6026	+8.51
CV-ORB	.1323	+8.49	.1856	+10.87	.1748	+11.34	.4171	+18.88
CV-FREAK	.2532	+11.36	.3204	+18.18	.3053	+14.93	.5574	+19.79
L2-Net	.4377	-5.27	.5012	-5.35	.4937	-5.99	.6951	+4.62
DoG-HardNet	.4427	-7.80	.5156	-6.98	.5056	-8.11	.7061	-.50
Key-Net-HardNet	.3081	-22.92	.4226	-15.23	.4012	-15.36	.6620	+2.11
GeoDesc	.4239	-2.05	.4924	-3.67	.4807	-4.93	.6956	+2.25
ContextDesc	.3976	-15.11	.4482	-12.09	.4535	-11.83	.6900	-1.91
SOSNet	.4439	-7.21	.5187	-7.15	.5073	-8.04	.7103	+1.18
LogPolarDesc	.4259	-6.89	.4898	-8.27	.4808	-8.22	.6871	-.82
D2-Net (SS)	.1231	-36.32	.1717	-22.95	.1608	-20.86	.4639	+0.89
D2-Net (MS)	.0998	-53.78	.1370	-45.33	.1316	-43.29	.4132	-13.02
R2D2 (wasf-n8-big)	.2218	-39.78	.3141	-29.21	.3032	-28.43	.6229	-8.83

Table 9 Test – Outlier pre-filtering with CNe (8k features). We report mAP at 10° with CNe, on stereo and multi-view, and its increase in performance w.r.t. Table 6 – positive Δ meaning CNe helps. When using CNe, we disable the ratio test.

	CV- $\sqrt{\text{SIFT}}$		HardNet		SOSNet		LogPolarDesc	
	NI \uparrow	mAA(10°) \uparrow	NI \uparrow	mAA(10°) \uparrow	NI \uparrow	mAA(10°) \uparrow	NI \uparrow	mAA(10°) \uparrow
Standard	281.7	0.4930	432.3	0.5543	424.6	0.5587	441.8	0.5340
Upright	270.0	0.4878	449.2	0.5542	432.9	0.5554	461.8	0.5409
Δ (%)	-4.15	-1.05	+3.91	-0.02	+1.95	-0.59	+4.53	+1.29
Upright++	358.9	0.5075	527.6	0.5728	508.4	0.5738	543.2	0.5510
Δ (%)	+27.41	+2.94	+22.04	+3.34	+19.74	+2.70	+22.95	+3.18

Table 10 Test – Stereo performance with upright descriptors (8k features). We report (NI) the number of inliers and mAA at 10° for the stereo task, using DEGENSAC. As DoG may return multiple orientations for the same point [55] (about 15%), we report: **(top)** with orientation estimation; **(middle)** setting the orientation to zero while removing duplicates; and **(bottom)** adding new points until hitting the 8k-feature budget.

	CV- $\sqrt{\text{SIFT}}$		HardNet		SOSNet		LogPolarDesc	
	NL \uparrow	mAA(10 $^\circ$) \uparrow	NL \uparrow	mAA(10 $^\circ$) \uparrow	NL \uparrow	mAA(10 $^\circ$) \uparrow	NL \uparrow	mAA(10 $^\circ$) \uparrow
Standard	3312.1	0.6765	4001.4	0.7096	3796.0	0.7021	4054.6	0.6928
Upright	3485.1	0.6572	3594.6	0.6962	4025.1	0.7054	3737.4	0.6934
Δ (%)	+5.22	-2.85	-10.17	-1.89	+6.04	+0.47	-7.82	+0.09
Upright++	4404.6	0.6792	4250.4	0.7231	3988.6	0.7129	4414.1	0.7109
Δ (%)	+32.99	+0.40	+6.22	+1.93	+5.07	+1.54	+8.87	+2.61

Table 11 Test – Multiview performance with upright descriptors (8k features). Analogous to Table 10, on the multiview task. We report the number of landmarks (NL) instead of the number of inliers (NI).

about 80% of the matches in a single forward pass, boosting mAA at 10° by 2-4% relative for stereo task and 8% for multiview task. In fact, it is surprising that nearly all classical methods benefit from it, with gains of up to 20% relative. By contrast, it damages performance with most learned descriptors, even those operating on DoG keypoints, and particularly for methods learned end-to-end, such as D2-Net and R2D2. We hypothesize this might be because the models performed better on the “classical” keypoints it was trained with – [97] reports that re-training them for a specific feature helps.

	CV- $\sqrt{\text{SIFT}}$		HardNet	SOSNet	D2Net			
	NI \uparrow	mAA(10 $^\circ$) \uparrow	NI \uparrow	mAA(10 $^\circ$) \uparrow	NI \uparrow	mAA(10 $^\circ$) \uparrow		
Exact	281.7	0.4930	432.0	0.5532	424.3	0.5575	470.6	0.2506
FLANN	274.6	0.4879	363.3	0.5222	339.8	0.5179	338.9	0.2046
Δ (%)	-2.52	-1.03	-15.90	-5.60	-19.92	-7.10	-27.99	-18.36

Table 12 Test – Stereo performance with OpenCV FLANN, using kd-tree approximate nearest neighbors (8k features). kd-tree parameters are: 4 trees, 128 checks. We report (NI) the number of inliers and mAA at 10° for the stereo task, using DEGENSAC.

6.5 On the effect of local feature orientation estimation — Tables 10 and 11

In contrast with classical methods, which estimate the orientation of each keypoint, modern, end-to-end pipelines [35, 38, 80] often skip this step, assuming that the images are roughly aligned (upright), with the descriptor shouldering the increased invariance requirements. As our images meet this condition, we experiment with setting the orientation of keypoints to a fixed value (zero). DoG often returns multiple orientations for the same keypoint, so we consider two variants: one where we simply remove keypoints which become duplicates after setting the orientation to a constant value (Upright), and a second one where we fill out the budget with new keypoints (Upright++). We list the results in Table 10, for stereo, and Table 11, for multiview. Performance increases across the board with Upright++ – albeit by a small margin.

6.6 On the effect of approximate nearest neighbor matching — Table 12

While it is known that approximate nearest neighbor search algorithms have non-perfect recall [67], it is not clear how their usage influences downstream performance. We thus compare exact (brute-force) nearest neighbor search with a popular choice for approximate nearest neighbor search, FLANN [67], as implemented in OpenCV. We experimented with different parameters and found that 4 trees and 128 checks provide a reasonable trade-off between precision and runtime. We report results with and without FLANN in Table 12. The performance drop varies for different methods: from a moderate 1% for RootSIFT, to 5-7% HardNet and SOSNet, and 18% for D2-Net.

6.7 Pose mAA vs. traditional metrics — Fig. 18

To examine the relationship between our pose metric and traditional metrics, we compare mAA against repeatability and matching score on the stereo task, with DEGENSAC. While the matching score seems to correlate with mAA, repeatability is harder to interpret. However, note that even for

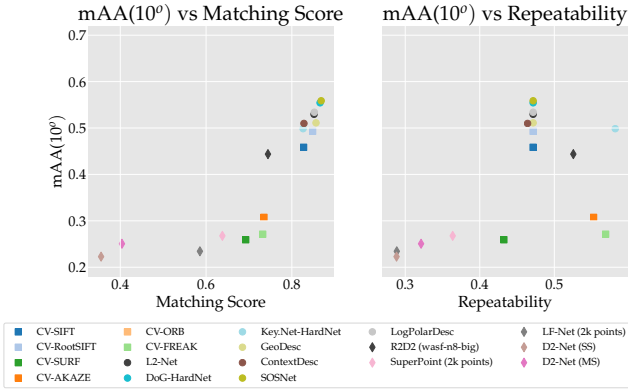


Fig. 18 Test – Downstream vs. traditional metrics. We cross-reference stereo mAA at 10° with repeatability and matching score, with a 3-pixel threshold.

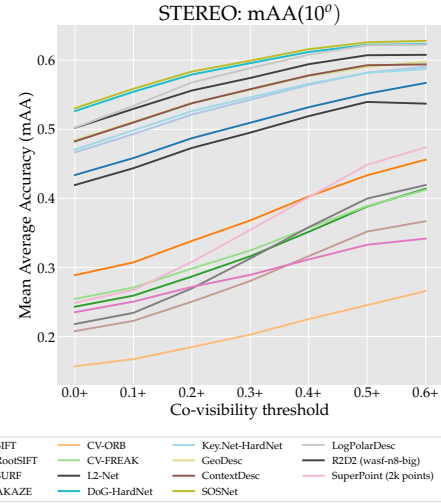


Fig. 20 Test – Local features vs. co-visibility. We plot mAA at 10° on the stereo task – using DEGENSAC – at different co-visibility thresholds for different local feature types. Bin “0+” consists of all possible image pairs, including potentially unmatchable ones. Bin “0.1+” includes pairs with a minimum co-visibility value of 0.1 – this is the default value we use for all other experiments in this paper – and so forth. Results are mostly consistent, with end-to-end methods performing better at higher than lower co-visibility.

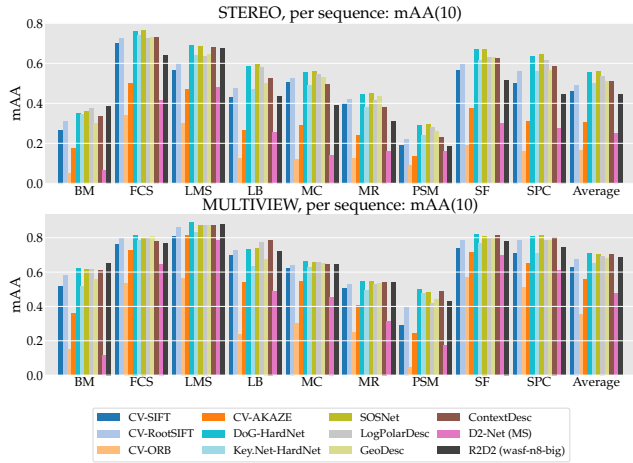


Fig. 19 Test – Breakdown by scene. For the stereo task, we use DEGENSAC. Note how performance can vary drastically between scenes, and the relative rank of a given local feature fluctuates as well. Please refer to Table 2 for a legend.

the matching score, which shows correlation, higher value does not guarantee high mAA – see *e.g.* RootSIFT vs ContextDesc. We remind the reader that, as explained in Section 4, our implementation differs from the classical formulation, as many methods do not have a strict notion of a support region. We compute these metrics at a 3-pixel threshold, and provide more granular results in Section 7.

As shown, all methods based on DoG are clustered, as they operate on the same keypoints. Key.Net obtains the best repeatability, but performs worse than DoG in terms of mAA with the same descriptors (HardNet). AKAZE and FREAK perform surprisingly well in terms of repeatability – #2 and #3, respectively – but obtain a low mAA, which may be related to their descriptors, which are binary. R2D2 shows good repeatability but a poor matching score and is outperformed by DoG-based features.

6.8 Breakdown by scene — Fig. 19

Results may vary drastically from scene to scene, as shown in Fig. 19. A given method may also perform better on some than others – for instance, D2-Net nears the state of the art on “Lincoln Memorial Statue”, but is 5x times worse on “British Museum”. AKAZE and ORB show similar behaviour. This can provide valuable insights on limitations and failure cases.

6.9 Breakdown by co-visibility — Figs. 20 and 21

Next, in Fig. 20 we evaluate stereo performance at different co-visibility thresholds, for several local feature methods, using DEGENSAC. Bins are encoded as $v+$, with v the co-visibility threshold, and include all image pairs with a co-visibility value larger or equal than v . This means that the first bin may contain unmatchable images – we use 0.1+ for all other experiments in the paper. We do not report values above 0.6+ as there are only a handful of them and thus the results are very noisy.

Performance for all local features and RANSAC variants increases with the co-visibility threshold, as expected. Results are consistent, with end-to-end methods performing better at higher than co-visibility than lower, and single-scale D2-Net outperforming its multi-scale counterpart at 0.4+ and above, where the images are more likely aligned in terms of scale.

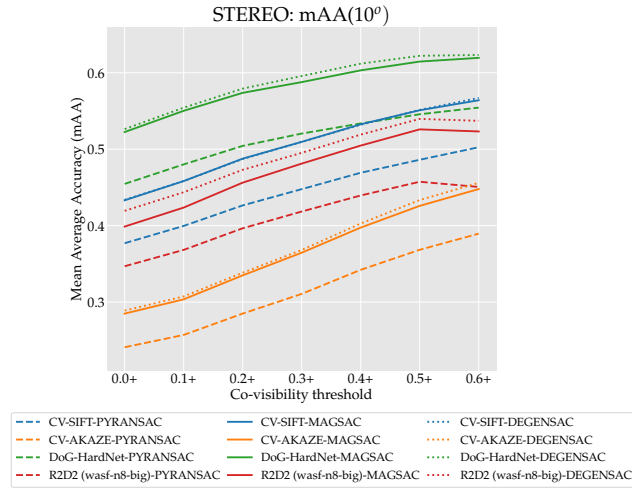


Fig. 21 Test – RANSAC vs. co-visibility. We plot mAA at 10° on the stereo task at different co-visibility thresholds for different RANSAC variants, binning the results as in Fig. 20. We pair them with different local features methods. The difference in performance between RANSAC variants seems consistent across pairs, regardless of their difficulty.

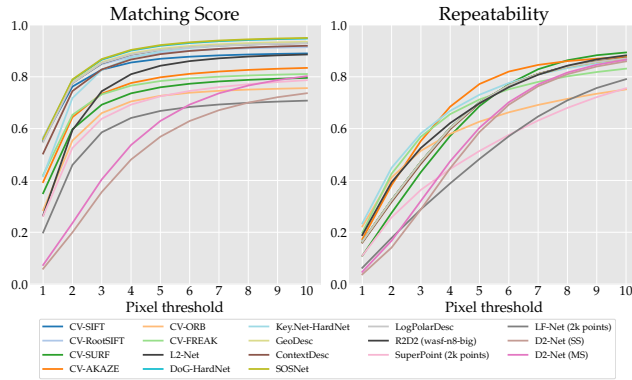


Fig. 22 Test – Classical metrics, by pixel threshold. We show repeatability and matching score computed at different pixel thresholds.

We also break down different RANSAC methods in Fig. 21, along with different local features, including AKAZE (binary), SIFT (also handcrafted), HardNet (learned descriptor on DoG points) and R2D2 (learned end-to-end). We do not observe significant variations in the trend of each curve as we swap RANSAC and local feature methods. DEGENSAC and MAGSAC show very similar performance.

6.10 Classical metrics vs. pixel threshold — Fig. 22

In Fig. 18 we plot repeatability and matching score against mAA at a fixed error threshold of 3 pixels. In Fig. 22 we show them at different pixel thresholds. End-to-end methods tend to perform better at higher pixel thresholds, which is expected – D2-Net in particular extracts keypoints from down-sampled feature maps. These results are computed from the

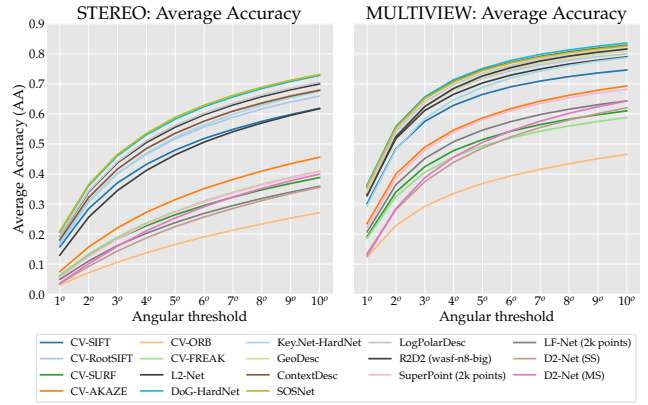


Fig. 23 Test – Breakdown by angular threshold, for local features. We evaluate the accuracy in pose estimation at every error threshold, rather than summarizing it by the mean Average Accuracy – which is the area under this curve. Ranks are consistent across thresholds.

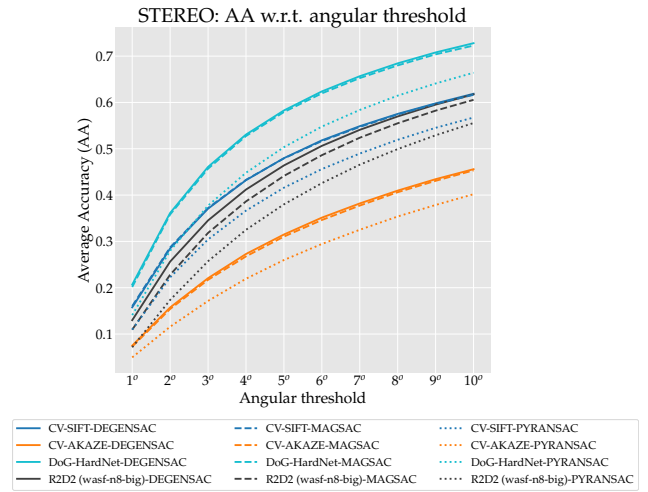


Fig. 24 Test – Breakdown by angular threshold, for RANSAC. We plot performance on the stereo task at different angular error thresholds, for four different local features and three RANSAC variants: MAGSAC (solid line), DEGENSAC (dashed line), and PYRANSAC (dotted line). We observe a similar behaviour across all thresholds.

depth maps estimated by COLMAP, which are not pixel-perfect, so the results for very low thresholds are not completely trustworthy.

Note that repeatability is typically lower than matching score, which might be counter-intuitive as the latter is more strict – it requires two features to be nearest-neighbors in descriptor space in addition to being physically close (after reprojection). We compute repeatability with the raw set of keypoints, whereas the matching score is computed with optimal matching settings – bidirectional matching with the “both” strategy and the ratio test. This results in a much smaller pool – 8k features are typically narrowed down to 200–400 matches (see Table 13). This better isolates the performance of the detector and the descriptor where it matters.

6.11 Breakdown by angular threshold — Figs. 23 and 24

We summarize pose accuracy by mAA at 10° in order to have a single, easy-to-interpret number. In this section we show how performance varies across different error thresholds – we look at the *average accuracy* at every angular error threshold, rather than the mean Average Accuracy. Fig. 23 plots performance on stereo and multiview for different local feature types, showing that the ranks remain consistent across thresholds. Fig. 24 shows how it affects different RANSAC variants, with four different local features. Again, ranks do not change. DEGENSAC and MAGSAC perform nearly identically for all features, except for R2D2. The consistency in the ranks demonstrate that summarizing the results with a single number, mAA at 10° , is reasonable.

6.12 Qualitative results — Figs. 27, 28, 29, and 30

Figs. 27 and 28 show qualitative results for the stereo task. We draw the inliers produced by DEGENSAC and color-code them using the ground truth depth maps, from green (0) to yellow (5 pixels off) if they are correct, and in red if they are incorrect (more than 5 pixels off). Matches including keypoints which fall on occluded pixels are drawn in blue. Note that while the depth maps are somewhat noisy and not pixel-accurate, they are sufficient for this purpose. Notice how the best performing methods have more correct matches that are well spread across the overlapping region.

Fig. 29 shows qualitative results for the multiview task, for handcrafted detectors. We illustrate it by simply drawing keypoints used in the SfM reconstruction in blue and the rest in red. It showcases the importance of the detector, specially on unmatchable regions such as the sky. ORB and Hessian keypoints are too concentrated in the high-contrast regions, failing to provide evenly-distributed features. In contrast, SURF fails to filter-out background and sky points. Fig. 30 shows results for learned methods: DoG+HardNet, Key.Net+HardNet, SuperPoint, R2D2, and D2-Net (multi-scale). They have different detection patterns: Key.Net resembles a “cleaned” version of DoG, while R2D2 seems to be evenly distributed. D2Net looks rather noisy, while SuperPoint fires precisely on corner points on structured parts, and sometimes form a regular grid on sky-like homogeneous regions, which might be due to the method running out of locations to place points at – note however that the best results were obtained with larger NMS (non-maxima suppression) thresholds.

7 Further results and considerations

In this section we provide additional results on the validation set. These include a study of the typical outlier ratios un-

Method	# matches	# inliers	Ratio (%)	mAA(10°)
CV-SIFT	328.3	113.0	34.4	0.548
CV- $\sqrt{\text{SIFT}}$	331.6	131.4	39.6	0.584
CV-SURF	221.5	77.4	35.0	0.309
CV-AKAZE	369.1	143.5	38.9	0.360
CV-ORB	193.4	74.7	38.6	0.265
CV-FREAK	216.6	75.5	34.8	0.329
DoG-HardNet	433.1	173.1	40.0	0.627
Key.Net-HardNet	644.1	166.6	25.9	0.580
L2Net	368.0	144.0	39.1	0.601
GeoDesc	322.6	133.4	41.3	0.564
ContextDesc	560.8	165.9	29.6	0.587
SOSNet	391.7	161.8	41.3	0.621
LogPolarDesc	522.8	175.2	33.5	0.618
SuperPoint (2k points)	202.0	62.6	31.0	0.312
LF-Net (2k points)	165.9	73.2	44.1	0.293
D2-Net (SS)	657.3	148.9	22.7	0.263
D2-Net (MS)	601.7	161.7	26.9	0.343
R2D2 (wasf-n8-big)	901.5	477.3	52.9	0.473

Table 13 Validation – Number of inliers with optimal settings. We use 8k features with optimal parameters, and PyRANSAC as a robust estimator. The number of inliers varies significantly between methods, despite tuning the matcher and the ratio test, and lower inlier ratios tend to correlate with low performance.

der optimal settings in Section 7.1, matching with FGINN in Section 7.2, image-preprocessing techniques for feature extraction in Section 7.3, and a breakdown of the optimal settings in Section 7.4, provided to serve as a reference.

7.1 Number of inliers per step — Table 13

We list the number of input matches and their *resulting* inliers for the stereo task, in Table 13. As before, we remind the reader that these inliers are what each method reports, *i.e.*, the matches that are actually used to estimate the poses. We list the number of input matches, the number of inliers produced by each method (which may still contain outliers), their ratio, and the mAA at 10° . We use PyRANSAC with optimal settings for each method, the ratio test, and bidirectional matching with the “both” strategy.

We see that inlier-to-outlier ratios hover around 35–40% for all features relying on classical detectors. Key.Net with HardNet descriptors sees a significant drop in inlier ratio and mAA, when compared to its DoG counterpart. D2-Net similarly has inlier ratios around 25%. R2D2 has the largest inlier ratio by far at 53%, but is outperformed by many other methods in terms of mAA, suggesting that many of these are not actual inliers. In general, we observe that the methods which produce a large number of matches, such as Key.Net (600+), D2-Net (600+) or R2D2 (900+) are less accurate in terms of pose estimation.

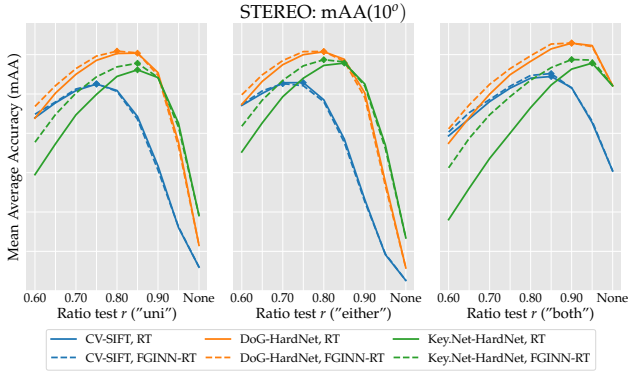


Fig. 25 Validation – FGINN vs. ratio test. We evaluate the ratio test with FGINN [65] (dashed line), and the standard ratio test (solid line). With FGINN, the valid range for r – the ratio test threshold – is significantly wider, but the best performance with the “both” matching strategy is not significantly better than for the standard ratio test.

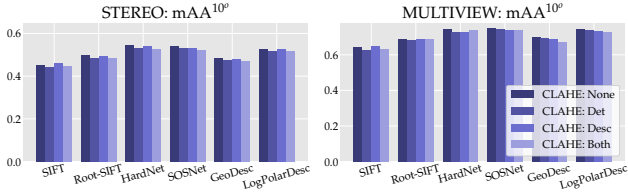


Fig. 26 Validation – Image pre-processing with CLAHE. We experiment with contrast normalization for keypoint and descriptor extraction. Results are very similar with or without it.

7.2 Feature matching with an advanced ratio test — Fig. 25

We also compare the benefits of applying first-geometrically-inconsistent-neighbor-ratio (FGINN) [65] to DoG/SIFT, DoG/HardNet and Key.Net/HardNet, against Lowe’s standard ratio test [55]. FGINN performs the ratio-test with second-nearest neighbors that are “far enough” from the tentative match (10 pixels in [65]). In other words, it loosens the test to allow for nearby-thus-similar points. We test it for 3 matching strategies: unidirectional (“uni”), “both” and “either”. We report the results in Fig. 25. As shown, FGINN provides minor improvements over the standard ratio test in case of unidirectional matching, and not as much when “both” is used. It also behaves differently compared to the standard strategy, in that performance at stricter thresholds degrades less.

7.3 Image pre-processing — Fig. 26

Contrast normalization is key to invariance against illumination changes – local feature methods typically apply some normalization strategy over small patches [55,64]. Therefore, we experiment with contrast-limited adaptive histogram equalization (CLAHE) [74], as implemented in OpenCV. We apply it to SIFT and to several learned descriptors, and display the results in Fig. 26. Performance

	η_{PyR}	η_{DEGEN}	η_{GCR}	η_{MAG}	r_{stereo}	$r_{\text{multiview}}$
CV-SIFT	0.25	0.5	0.5	1.25	0.85	0.75
CV- $\sqrt{\text{SIFT}}$	0.25	0.5	0.5	1.25	0.85	0.85
CV-SURF	0.75	0.75	0.75	2	0.85	0.90
CV-AKAZE	0.25	0.75	0.75	1.5	0.85	0.90
CV-ORB	0.75	1	1.25	2	0.85	0.95
CV-FREAK	0.5	0.5	0.75	2	0.85	0.85
VL-DoG-SIFT	0.25	0.5	0.5	1.5	0.85	0.80
VL-DoGAff-SIFT	0.25	0.5	0.5	1.5	0.85	0.80
VL-Hess-SIFT	0.2	0.5	0.5	1.5	0.85	0.80
VL-HessAffNet-SIFT	0.25	0.5	0.5	1	0.85	0.80
CV-DoG/HardNet	0.25	0.5	0.5	1.5	0.90	0.80
KeyNet/HardNet	0.5	0.75	0.75	2	0.95	0.85
CV-DoG/L2Net	0.2	0.5	0.5	1.5	0.90	0.80
CV-DoG/GeoDesc	0.2	0.5	0.75	1.5	0.90	0.85
ContextDesc	0.25	0.75	0.5	1	0.95	0.85
CV-DoG/SOSNet	0.25	0.5	0.75	1.5	0.90	0.80
CV-DoG/LogPolarDesc	0.2	0.5	0.5	1.5	0.90	0.80
D2-Net (SS)	1	2	2	7.5	—	—
D2-Net (MS)	1	2	2	5	—	—
R2D2 (wasf-n8-big)	0.75	1.25	1.25	2	—	0.95

Table 14 Optimal hyper-parameters with 8k features. We summarize the optimal hyperparameters – the maximum number of RANSAC iterations η and the ratio test threshold r – for each combination of methods. The number of RANSAC iterations Γ is set to 250k for Py-RANSAC, 50k for DEGENSAC, and 10k for both GC-RANSAC and MAGSAC (for the experiments on the validation set). We use bidirectional matching with the “both” strategy.

decreases for all learned methods, presumably because they are not trained for it. Contrary to our initial expectations, SIFT does not benefit much from it either: the only increase in performance comes from applying it for descriptor extraction, at 2.5% relative for stereo task and 0.56% relative for multi-view. This might be due to the small number of night-time images in our data. It also falls in line with the observations in [36], which show that SIFT descriptors are actually optimal under certain assumptions.

7.4 Optimal settings breakdown — Tables 14 and 15

For the sake of clarity, we summarize the optimal hyperparameter combinations from Figs. 8, 9 and 10 in Table 14 (for 8k features) and Table 15 (for 2k features). We set the confidence value to $\tau=0.999999$ for all RANSAC variants. Notice how it is better to have more features and a stricter ratio test threshold to filter them out, than having fewer features from the beginning.

8 Conclusions

We introduce a comprehensive benchmark for local features and robust estimation algorithms. The modular structure of its pipeline allows to easily integrate, configure, and combine methods and heuristics. We demonstrate this by evaluating dozens of popular algorithms, from seminal works to the cutting edge of machine learning research, and show that



Fig. 27 Qualitative results for the stereo task – “Classical” features. We plot the matches predicted by each local feature, with DEGENSAC. Matches above a 5-pixel error threshold are drawn in **red**, and those below are color-coded by their error, from 0 (**green**) to 5 pixels (**yellow**). Matches for which we do not have depth estimates are drawn in **blue**.

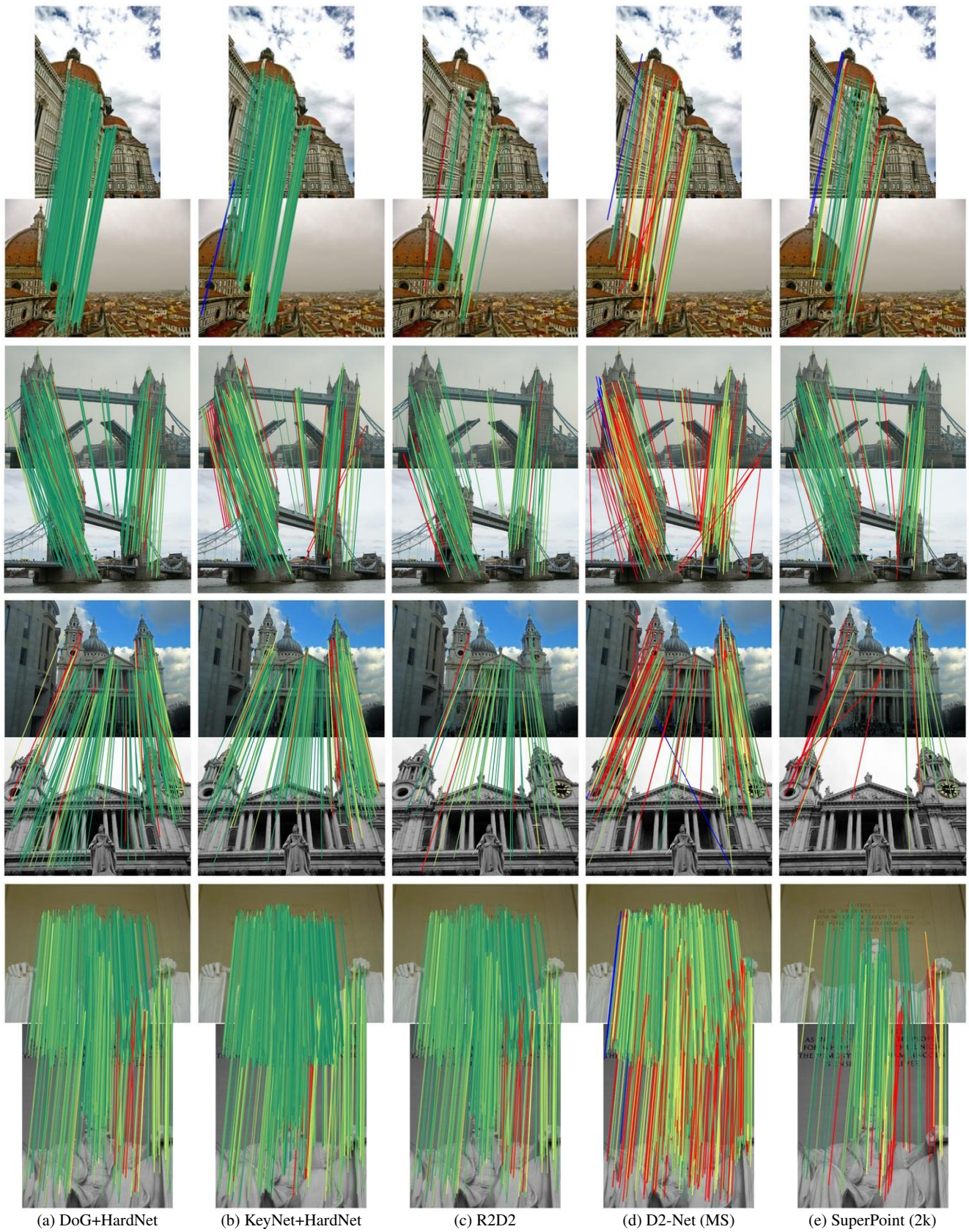


Fig. 28 Qualitative results for the stereo task – Learned features. Color-coded as in Fig. 27.

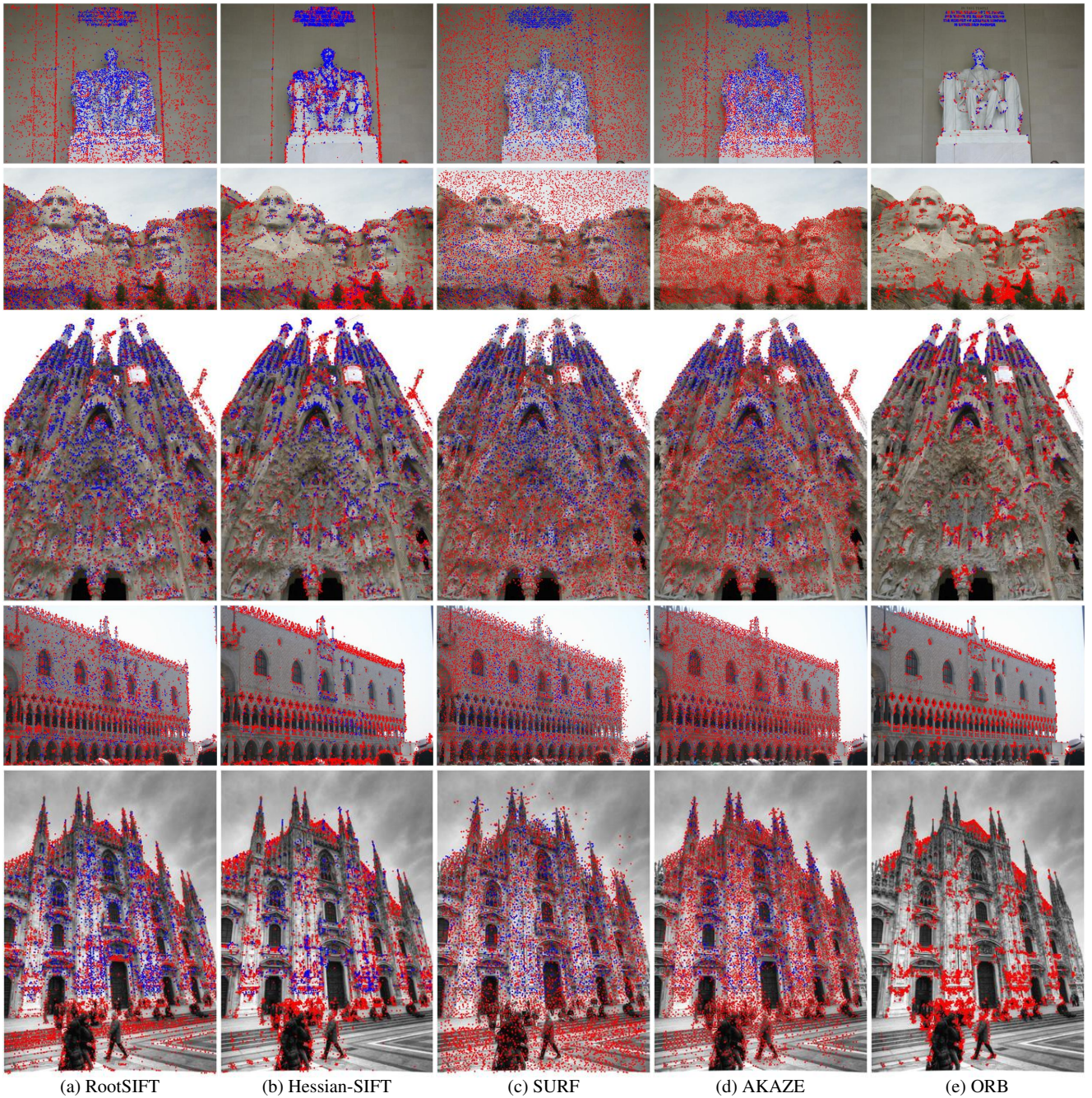


Fig. 29 Qualitative results for the multi-view task – “Classical” features. We show images and the keypoints detected on them for different methods, with the points reconstructed by COLMAP in **blue**, and the ones that are not used in the 3D model in **red** – more blue points indicate denser 3D models. These results correspond the multiview-task for a 25-image subset.

classical solutions may still outperform the perceived state of the art with proper settings.

The experiments carried out through the benchmark and reported in this paper have already revealed unexpected, non-intuitive properties of various components of the SfM pipeline, which will benefit SfM development, *e.g.*, the need to tune RANSAC to the particular feature detector *and* descriptor and to select specific settings for a particular RAN-

SAC variant. Other interesting facts have been uncovered by our tests, such as that the optimal set-ups across different tasks (stereo and multiview) may differ, or that methods that perform better on proxy tasks, like patch retrieval or repeatability, may be inferior on the downstream task. Our work is open-sourced and makes the basis of an open challenge for image matching with sparse methods.



Fig. 30 Qualitative results for the multi-view task – Learned features. Color-coded as in Fig. 29.

9 Differences with the previous arXiv version

An earlier version of the paper is available as a technical report on arXiv. Some results in this version are different from it – this section briefly highlights the most significant differences, for the curious reader.

- We removed the “Reichstag” scene from the test set. It contained fewer than 100 images, and thus could not be subsampled – the ground truth could thus be triv-

ially reconstructed from the released images, which goes against our decision of keeping the ground truth for the test set private. We have reformatted it into an additional – optional – validation scene, which is not used in this paper.

- We removed the “United States Capitol” scene from the test set. It contained a nearly perfectly symmetrical structure (a capitol building), which caused a few reg-

	η_{PyR}	η_{DEGEN}	η_{MAG}	r_{stereo}	$r_{\text{multiview}}$
CV-SIFT	0.75	0.5	2	0.90	0.90
CV- $\sqrt{\text{SIFT}}$	0.5	0.5	1.25	0.90	0.90
CV-SURF	0.25	1	3	0.90	0.95
CV-AKAZE	1	0.75	2	0.90	0.95
CV-ORB	1	1.25	3	0.90	0.90
CV-FREAK	0.75	0.75	2	0.9	0.95
CV-DoG/HardNet	0.5	0.5	1.5	0.95	0.90
KeyNet/HardNet	0.5	0.75	2.5	0.95	0.90
CV-DoG/L2Net	0.25	0.5	1.5	0.90	0.90
CV-DoG/GeoDesc	0.5	0.5	1.5	0.95	0.90
ContextDesc	0.75	0.75	2	0.95	0.95
CV-DoG/SOSNet	0.5	0.75	1.5	0.95	0.90
CV-DoG/LogPolarDesc	0.5	0.5	1.5	0.95	0.90
D2-Net (SS)	1.5	2	7.5	—	—
D2-Net (MS)	1.5	2	10	—	—
SuperPoint	0.75	1	3	0.95	0.90
LF-Net	1	1	4	0.95	0.95
R2D2 (wasf-n16)	1.5	1.25	2	—	—

Table 15 Optimal hyper-parameters with 2k features. Equivalent to Table 14. We do not evaluate GC-RANSAC, as it is always outperformed by DEGENSAC and MAGSAC, but keep PyRANSAC as a baseline RANSAC.

istration errors, despite the fact that the scene contained hundreds of images – a shortcoming of SfM.

- As stated in Section 3.3, we inspected every image in the test set manually to confirm they were correctly registered by COLMAP, and found four images in “London Bridge” that were not. We removed them from our test set.
- For the multiview task, we had an additional category containing subsets of 3 images (along with 5, 10, and 25). We deemed this too small and noisy – results were drastically lower than for the 5-image sets – and removed it from the test set. This explains why multiview performance is typically higher than stereo performance, whereas the previous version reports the opposite.
- The previous results were obtained with OpenCV FLANN approximate nearest neighbor search. We found that it influences the results quite significantly (up to 18% relative) and re-ran all the experiments on the test set using exact matching.
- For consistency with the challenge, the results on the test set are computed three times (for both stereo and multiview) and averaged. Results on the validation set use a single run to keep computation manageable.

References

1. H. Aanaes, A. L. Dahl, and K. Steenstrup Pedersen. Interesting Interest Points. *IJCV*, 97:18–35, 2012. 3
2. H. Aanaes and F. Kahl. Estimation of Deformable Structure and Motion. In *Vision and Modelling of Dynamic Scenes Workshop*, 2002. 12
3. S. Agarwal, N. Snavely, I. Simon, S.M. Seitz, and R. Szeliski. Building Rome in One Day. In *ICCV*, 2009. 2, 3
4. A. Alahi, R. Ortiz, and P. Vanderghenst. FREAK: Fast Retina Keypoint. In *CVPR*, 2012. 7, 11
5. P. F. Alcantarilla, J. Nuevo, and A. Bartoli. Fast Explicit Diffusion for Accelerated Features in Nonlinear Scale Spaces. In *BMVC*, 2013. 2, 7, 11
6. Javier Aldana-Luit, Dmytro Mishkin, Ondej Chum, and Ji Matas. Saddle: Fast and repeatable features with good coverage. *Image and Vision Computing*, 2019. 12
7. Anonymous. DeepSfM: Structure From Motion Via Deep Bundle Adjustment. In *Submission to ICLR*, 2020. 2
8. Relja Arandjelovic. Three things everyone should know to improve object retrieval. In *CVPR*, 2012. 7
9. Relja Arandjelovic, Petr Gronat, Akihiko Torii, Tomas Pajdla, and Josef Sivic. NetVLAD: CNN Architecture for Weakly Supervised Place Recognition. In *CVPR*, 2016. 2
10. Hernan Badino, Daniel Huber, and Takeo Kanade. The CMU Visual Localization Data Set. <http://3dvis.rti.cmu.edu/data-sets/localization>, 2011. 3
11. V. Balntas, K. Lenc, A. Vedaldi, and K. Mikolajczyk. HPatches: A Benchmark and Evaluation of Handcrafted and Learned Local Descriptors. In *CVPR*, 2017. 3, 4, 11, 13
12. Vassileios Balntas, Shuda Li, and Victor Prisacariu. RelocNet: Continuous Metric Learning Relocalisation using Neural Nets. In *The European Conference on Computer Vision (ECCV)*, September 2018. 2
13. V. Balntas, E. Riba, D. Ponsa, and K. Mikolajczyk. Learning Local Feature Descriptors with Triplets and Shallow Convolutional Neural Networks. In *BMVC*, 2016. 2
14. Daniel Barath and Ji Matas. Graph-cut ransac. In *The IEEE Conference on Computer Vision and Pattern Recognition (CVPR)*, June 2018. 3, 8
15. Axel Barroso-Laguna, Edgar Riba, Daniel Ponsa, and Krystian Mikolajczyk. Key.Net: Keypoint Detection by Handcrafted and Learned CNN Filters. In *Proceedings of the 2019 IEEE/CVF International Conference on Computer Vision*, 2019. 2, 8
16. A. Baumberg. Reliable Feature Matching Across Widely Separated Views. In *CVPR*, pages 774–781, 2000. 7, 12
17. H. Bay, T. Tuytelaars, and L. Van Gool. SURF: Speeded Up Robust Features. In *ECCV*, 2006. 2, 7
18. P. R. Beaudet. Rotationally invariant image operators. In *Proceedings of the 4th International Joint Conference on Pattern Recognition*, pages 579–583, Kyoto, Japan, Nov. 1978. 7, 12
19. Fabio Bellavia and Carlo Colombo. Is there anything new to say about sift matching? *International Journal of Computer Vision*, pages 1–20, 2020. 8
20. Jia-Wang Bian, Yu-Huan Wu, Ji Zhao, Yun Liu, Le Zhang, Ming-Ming Cheng, and Ian Reid. An Evaluation of Feature Matchers for Fundamental Matrix Estimation. In *BMVC*, 2019. 4
21. Eric Brachmann and Carsten Rother. Neural- Guided RANSAC: Learning Where to Sample Model Hypotheses. In *ICCV*, 2019. 2
22. G. Bradski. The OpenCV Library. *Dr. Dobbs Journal of Software Tools*, 2000. 8
23. M. Brown, G. Hua, and S. Winder. Discriminative Learning of Local Image Descriptors. *PAMI*, 2011. 2, 13
24. M. Brown and D. Lowe. Automatic Panoramic Image Stitching Using Invariant Features. *IJCV*, 74:59–73, 2007. 3
25. Mai Bui, Christoph Baur, Nassir Navab, Slobodan Ilic, and Shadi Albarqouni. Adversarial Networks for Camera Pose Regression and Refinement. In *The IEEE International Conference on Computer Vision (ICCV) Workshops*, Oct 2019. 2
26. Ondřej Chum and Jiří Matas. Matching with PROSAC - Progressive Sample Consensus. In *CVPR*, pages 220–226, June 2005. 3
27. Ondřej Chum, Jiří Matas, and Josef Kittler. Locally Optimized RANSAC. In *PR*, 2003. 3
28. Ondřej Chum, Jiří Matas, and Josef Kittler. Locally optimized ransac. In *Pattern Recognition*, 2003. 8

29. Ondrej Chum, Tomas Werner, and Jiri Matas. Two-View Geometry Estimation Unaffected by a Dominant Plane. In *CVPR*, 2005. 3, 8
30. Hainan Cui, Xiang Gao, Shuhan Shen, and Zhanyi Hu. Hsfm: Hybrid structure-from-motion. In *CVPR*, July 2017. 3
31. Zheng Dang, Kwang Moo Yi, Yinlin Hu, Fei Wang, Pascal Fua, and Mathieu Salzmann. Eigendecomposition-Free Training of Deep Networks with Zero Eigenvalue-Based Losses. In *ECCV*, 2018. 8
32. Jana Noskova Daniel Barath, Jiri Matas. MAGSAC: marginalizing sample consensus. In *CVPR*, 2019. 1, 3, 8
33. D. Detone, T. Malisiewicz, and A. Rabinovich. Toward Geometric Deep SLAM. *arXiv preprint arXiv:1707.07410*, 2017. 2
34. D. Detone, T. Malisiewicz, and A. Rabinovich. Self-Improving Visual Odometry. *arXiv Preprint*, 2018. 6
35. D. Detone, T. Malisiewicz, and A. Rabinovich. Superpoint: Self-Supervised Interest Point Detection and Description. *CVPR Workshop on Deep Learning for Visual SLAM*, 2018. 2, 8, 15
36. Jingming Dong, Nikolaos Karianakis, Damek Davis, Joshua Hernandez, Jonathan Balzer, and Stefano Soatto. Multi-view feature engineering and learning. In *CVPR*, June 2015. 19
37. J. Dong and S. Soatto. Domain-Size Pooling in Local Descriptors: DSP-SIFT. In *CVPR*, 2015. 12
38. M. Dusmanu, I. Rocco, T. Pajdla, M. Pollefeys, J. Sivic, A. Torii, and T. Sattler. D2-Net: A Trainable CNN for Joint Detection and Description of Local Features. In *CVPR*, 2019. 1, 2, 7, 8, 15
39. Patrick Ebel, Anastasiia Mishchuk, Kwang Moo Yi, Pascal Fua, and Eduard Trulls. Beyond Cartesian Representations for Local Descriptors. In *ICCV*, 2019. 2, 7, 8, 12
40. Vassileios Balntas et al. SILDA: A Multi-Task Dataset for Evaluating Visual Localization. <https://github.com/scape-research/silda>, 2018. 3, 4
41. M.A Fischler and R.C. Bolles. Random Sample Consensus: A Paradigm for Model Fitting with Applications to Image Analysis and Automated Cartography. *Communications ACM*, 24(6):381–395, 1981. 2, 3, 8
42. P. Gay, V. Bansal, C. Rubino, and A. D. Bue. Probabilistic Structure from Motion with Objects (PSfMO). In *ICCV*, 2017. 3
43. Andreas Geiger, Philip Lenz, and Raquel Urtasun. Are we ready for Autonomous Driving? The KITTI Vision Benchmark Suite. In *CVPR*, 2012. 3
44. R.I. Hartley. In Defense of the Eight-Point Algorithm. *PAMI*, 19(6):580–593, June 1997. 3
45. R. Hartley and A. Zisserman. *Multiple View Geometry in Computer Vision*. Cambridge University Press, 2000. 2, 9
46. R. I. Hartley. Projective reconstruction and invariants from multiple images. *IEEE Transactions on Pattern Analysis and Machine Intelligence*, 16(10):1036–1041, Oct 1994. 2, 3
47. K. He, Y. Lu, and S. Sclaroff. Local Descriptors Optimized for Average Precision. In *CVPR*, 2018. 2
48. J. Heinly, J.L. Schoenberger, E. Dunn, and J-M. Frahm. Reconstructing the World in Six Days. In *CVPR*, 2015. 2, 3, 4
49. N. Jacobs, N. Roman, and R. Pless. Consistent Temporal Variations in Many Outdoor Scenes. In *CVPR*, 2007. 3
50. Karel Lenc and Varun Gulshan and Andrea Vedaldi. VLBenchmarks. <http://www.vlfeat.org/benchmarks/>, 2011. 4
51. A. Kendall, M. Grimes, and R. Cipolla. Posenet: A Convolutional Network for Real-Time 6-DOF Camera Relocalization. In *ICCV*, pages 2938–2946, 2015. 2
52. J. Krishna Murthy, Ganesh Iyer, and Liam Paull. gradSLAM: Dense SLAM meets Automatic Differentiation. *arXiv*, 2019. 2
53. S. Leutenegger, M. Chli, and R. Y. Siegwart. Brisk: Binary robust invariant scalable keypoints. In *ICCV*, pages 2548–2555, 2011. 7
54. Zhengqi Li and Noah Snavely. MegaDepth: Learning Single-View Depth Prediction from Internet Photos. In *CVPR*, 2018. 4
55. David G. Lowe. Distinctive Image Features from Scale-Invariant Keypoints. *IJCV*, 20(2):91–110, November 2004. 1, 2, 6, 7, 8, 12, 15, 19
56. Zixin Luo, Tianwei Shen, Lei Zhou, Jiahui Zhang, Yao Yao, Shiwei Li, Tian Fang, and Long Quan. ContextDesc: Local Descriptor Augmentation with Cross-Modality Context. In *CVPR*, 2019. 2, 8
57. Z. Luo, T. Shen, L. Zhou, S. Zhu, R. Zhang, Y. Yao, T. Fang, and L. Quan. Geodesc: Learning Local Descriptors by Integrating Geometry Constraints. In *ECCV*, 2018. 2, 8
58. Simon Lynen, Bernhard Zeisl, Dror Aiger, Michael Bosse, Joel Hesch, Marc Pollefeys, Roland Siegwart, and Torsten Sattler. Large-scale, real-time visual-inertial localization revisited. *arXiv Preprint*, 2019. 2
59. Will Maddern, Geoffrey Pascoe, Chris Linegar, and Paul Newman. 1 year, 1000 km: The Oxford RobotCar dataset. *IJRR*, 36(1):3–15, 2017. 3
60. J. Matas, O. Chum, M. Urban, and T. Pajdla. Robust Wide-Baseline Stereo from Maximally Stable Extremal Regions. *IVC*, 22(10):761–767, 2004. 7, 12
61. K. Mikolajczyk and C. Schmid. A Performance Evaluation of Local Descriptors. *PAMI*, 27(10):1615–1630, 2004. 3, 11
62. K. Mikolajczyk, C. Schmid, and A. Zisserman. Human Detection Based on a Probabilistic Assembly of Robust Part Detectors. In *ECCV*, pages 69–82, 2004. 7, 12
63. Jiri Matas Milan Pultar, Dmytro Mishkin. Leveraging Outdoor Webcams for Local Descriptor Learning. In *Proceedings of CVWW 2019*, 2019. 13
64. A. Mishchuk, D. Mishkin, F. Radenovic, and J. Matas. Working Hard to Know Your Neighbor’s Margins: Local Descriptor Learning Loss. In *NeurIPS*, 2017. 2, 8, 12, 19
65. Dmytro Mishkin, Jiri Matas, and Michal Perdoch. MODS: Fast and robust method for two-view matching. *CVIU*, 2015. 11, 19
66. D. Mishkin, F. Radenovic, and J. Matas. Repeatability is Not Enough: Learning Affine Regions via Discriminability. In *ECCV*, 2018. 7, 12
67. Marius Muja and David G. Lowe. Fast Approximate Nearest Neighbors with Automatic Algorithm Configuration. In *ICCV*, 2009. 15
68. Arun Mukundan, Giorgos Toliass, and Ondrej Chum. Explicit Spatial Encoding for Deep Local Descriptors. In *CVPR*, 2019. 2
69. R. Mur-Artal, J. Montiel, and J. Tardós. Orb-Slam: A Versatile and Accurate Monocular Slam System. *IEEE Transactions on Robotics*, 31(5):1147–1163, 2015. 2
70. D. Nister. An Efficient Solution to the Five-Point Relative Pose Problem. In *CVPR*, June 2003. 3
71. Hyeonwoo Noh, Andre Araujo, Jack Sim, and Tobias Weyand and Bohyung Han. Large-Scale Image Retrieval with Attentive Deep Local Features. In *ICCV*, 2017. 2
72. Yuki Ono, Eduard Trulls, Pascal Fua, and Kwang Moo Yi. LF-Net: Learning Local Features from Images. In *NeurIPS*, 2018. 2, 7, 8
73. F. Pedregosa, G. Varoquaux, A. Gramfort, V. Michel, B. Thirion, O. Grisel, M. Blondel, P. Prettenhofer, R. Weiss, V. Dubourg, J. Vanderplas, A. Passos, D. Cournapeau, M. Brucher, M. Perrot, and E. Duchesnay. Scikit-learn: Machine learning in Python. *Journal of Machine Learning Research*, 12:2825–2830, 2011. 8
74. Stephen M. Pizer, E. Philip Amburn, John D. Austin, Robert Cromartie, Ari Geselowitz, Trey Greer, Bart ter Haar Romeny, John B. Zimmerman, and Karel Zuiderveld. Adaptive histogram equalization and its variations. *Computer vision, graphics, and image processing*, 1987. 19
75. Phil Pritchett and Andrew Zisserman. Wide baseline stereo matching. In *ICCV*, pages 754–760, 1998. 2
76. M. Pultar, D. Mishkin, and J. Matas. Leveraging Outdoor Webcams for Local Descriptor Learning. In *Computer Vision Winter Workshop*, 2019. 3
77. C.R. Qi, H. Su, K. Mo, and L.J. Guibas. Pointnet: Deep Learning on Point Sets for 3D Classification and Segmentation. In *CVPR*, 2017. 8

78. Filip Radenovic, Georgios Tolas, and Ondrej Chum. CNN image retrieval learns from BoW: Unsupervised fine-tuning with hard examples. In *ECCV*, 2016. [2](#)
79. R. Ranftl and V. Koltun. Deep Fundamental Matrix Estimation. In *ECCV*, 2018. [2](#), [3](#), [7](#), [8](#)
80. J. Revaud, P. Weinzaepfel, C. De Souza, N. Pion, G. Csurka, Y. Cabon, and M. Humenberger. R2D2: Repeatable and Reliable Detector and Descriptor. In *arXiv Preprint*, 2019. [6](#), [8](#), [15](#)
81. Jérôme Revaud, Philippe Weinzaepfel, César Roberto de Souza, Noe Pion, Gabriela Csurka, Yohann Cabon, and Martin Humenberger. R2D2: Repeatable and Reliable Detector and Descriptor. In *NeurIPS*, 2019. [2](#)
82. E. Rosten, R. Porter, and T. Drummond. Faster and Better: A Machine Learning Approach to Corner Detection. *PAMI*, 32:105–119, 2010. [9](#)
83. E. Rublee, V. Rabaud, K. Konolidge, and G. Bradski. ORB: An Efficient Alternative to SIFT or SURF. In *ICCV*, 2011. [2](#), [7](#), [11](#)
84. Paul-Edouard Sarlin, Daniel DeTone, Tomasz Malisiewicz, and Andrew Rabinovich. Superglue: Learning feature matching with graph neural networks. In *CVPR*, 2020. [7](#)
85. Torsten Sattler, Bastian Leibe, and Leif Kobbelt. Improving Image-Based Localization by Active Correspondence Search. In *ECCV*, 2012. [2](#), [3](#), [11](#)
86. T. Sattler, W. Maddern, C. Toft, A. Torii, L. Hammarstrand, E. Stenborg, D. Safari, M. Okutomi, M. Pollefeys, J. Sivic, F. Kahl, and T. Pajdla. Benchmarking 6DOF Outdoor Visual Localization in Changing Conditions. In *CVPR*, 2018. [2](#), [3](#)
87. Torsten Sattler, Tobias Weyand, Bastian Leibe, and Leif Kobbelt. Image Retrieval for Image-Based Localization Revisited. In *BMVC*, 2012. [3](#)
88. Torsten Sattler, Qunjie Zhou, Marc Pollefeys, and Laura Leal-Taixe. Understanding the Limitations of CNN-based Absolute Camera Pose Regression. In *CVPR*, 2019. [2](#)
89. N. Savinov, A. Seki, L. Ladicky, T. Sattler, and M. Pollefeys. Quad-Networks: Unsupervised Learning to Rank for Interest Point Detection. *CVPR*, 2017. [2](#)
90. J.L. Schönberger and J.M. Frahm. Structure-From-Motion Revisited. In *CVPR*, 2016. [2](#), [3](#), [4](#), [8](#), [11](#)
91. J.L. Schönberger, H. Hardmeier, T. Sattler, and M. Pollefeys. Comparative Evaluation of Hand-Crafted and Learned Local Features. In *CVPR*, 2017. [4](#)
92. J.L. Schönberger, E. Zheng, M. Pollefeys, and J.M. Frahm. Pixelwise View Selection for Unstructured Multi-View Stereo. In *ECCV*, 2016. [4](#)
93. Yunxiao Shi, Jing Zhu, Yi Fang, Kuochin Lien, and Junli Gu. Self-Supervised Learning of Depth and Ego-motion with Differentiable Bundle Adjustment. *arXiv Preprint*, 2019. [2](#)
94. E. Simo-serra, E. Trulls, L. Ferraz, I. Kokkinos, P. Fua, and F. Moreno-Noguer. Discriminative Learning of Deep Convolutional Feature Point Descriptors. In *ICCV*, 2015. [2](#)
95. C. Strecha, W.V. Hansen, L. Van Gool, P. Fua, and U. Thoennessen. On Benchmarking Camera Calibration and Multi-View Stereo for High Resolution Imagery. In *CVPR*, 2008. [3](#), [4](#)
96. J. Sturm, N. Engelhard, F. Endres, W. Burgard, and D. Cremers. A Benchmark for the Evaluation of RGB-D SLAM Systems. In *IROS*, 2012. [9](#)
97. Weiwei Sun, Wei Jiang, Eduard Trulls, Andrea Tagliasacchi, and Kwang Moo Yi. ACNe: Attentive Context Normalization for Robust Permutation-Equivariant Learning. In *CVPR*, 2020. [2](#), [3](#), [8](#), [15](#)
98. Hajime Taira, Masatoshi Okutomi, Torsten Sattler, Mircea Cimpoi, Marc Pollefeys, Josef Sivic, Tomas Pajdla, and Akihiko Torii. InLoc: Indoor Visual Localization with Dense Matching and View Synthesis. *PAMI*, 2019. [11](#)
99. Chengzhou Tang and Ping Tan. Ba-Net: Dense Bundle Adjustment Network. In *ICLR*, 2019. [2](#)
100. Keisuke Tateno, Federico Tombari, Iro Laina, and Nassir Navab. Cnn-slam: Real-time dense monocular slam with learned depth prediction. In *CVPR*, July 2017. [2](#)
101. B. Thomee, D.A. Shamma, G. Friedland, B. Elizalde, K. Ni, D. Poland, D. Borth, and L. Li. YFCC100M: the New Data in Multimedia Research. In *CACM*, 2016. [4](#)
102. Y. Tian, B. Fan, and F. Wu. L2-Net: Deep Learning of Discriminative Patch Descriptor in Euclidean Space. In *CVPR*, 2017. [2](#), [8](#)
103. Yurun Tian, Xin Yu, Bin Fan, Fuchao Wu, Huub Heijnen, and Vassileios Balntas. SOSNet: Second Order Similarity Regularization for Local Descriptor Learning. In *CVPR*, 2019. [2](#), [8](#)
104. Giorgos Tolas, Yannis Avrithis, and Hervé Jégou. Image Search with Selective Match Kernels: Aggregation Across Single and Multiple Images. *IJCV*, 116(3):247–261, Feb 2016. [2](#)
105. P.H.S. Torr and A. Zisserman. MLESAC: A New Robust Estimator with Application to Estimating Image Geometry. *CVIU*, 78:138–156, 2000. [3](#)
106. B. Triggs, P. McLauchlan, R. Hartley, and A. Fitzgibbon. Bundle Adjustment – A Modern Synthesis. In *Vision Algorithms: Theory and Practice*, pages 298–372, 2000. [2](#)
107. Andrea Vedaldi and Brian Fulkerson. VLFeat: An open and portable library of computer vision algorithms. In *Proceedings of the 18th ACM International Conference on Multimedia*, MM '10, pages 1469–1472, 2010. [7](#)
108. Y. Verdie, K. M. Yi, P. Fua, and V. Lepetit. TILDE: A Temporally Invariant Learned DETector. In *CVPR*, 2015. [2](#), [3](#)
109. S. Vijayanarasimhan, S. Ricco, C. Schmid, R. Sukthankar, and K. Fragkiadaki. Sfm-Net: Learning of Structure and Motion from Video. *arXiv Preprint*, 2017. [2](#)
110. X. Wei, Y. Zhang, Y. Gong, and N. Zheng. Kernelized Subspace Pooling for Deep Local Descriptors. In *CVPR*, 2018. [2](#)
111. Changchang Wu. Towards Linear-Time Incremental Structure from Motion. In *3DV*, 2013. [3](#), [11](#)
112. Kwang Moo Yi, Eduard Trulls, Vincent Lepetit, and Pascal Fua. LIFT: Learned Invariant Feature Transform. In *ECCV*, 2016. [2](#)
113. K. M. Yi, E. Trulls, Y. Ono, V. Lepetit, M. Salzmann, and P. Fua. Learning to Find Good Correspondences. In *CVPR*, 2018. [2](#), [3](#), [4](#), [5](#), [7](#), [8](#), [9](#), [14](#)
114. Andy B Yoo, Morris A Jette, and Mark Grondona. Slurm: Simple linux utility for resource management. In *Workshop on Job Scheduling Strategies for Parallel Processing*, pages 44–60. Springer, 2003. [9](#)
115. S. Zagoruyko and N. Komodakis. Learning to Compare Image Patches via Convolutional Neural Networks. In *CVPR*, 2015. [12](#)
116. Jiahui Zhang, Dawei Sun, Zixin Luo, Anbang Yao, Lei Zhou, Tianwei Shen, Yurong Chen, Long Quan, and Hongen Liao. Learning Two-View Correspondences and Geometry Using Order-Aware Network. *ICCV*, 2019. [2](#), [3](#), [5](#), [8](#)
117. Jiahui Zhang, Dawei Sun, Zixin Luo, Anbang Yao, Lei Zhou, Tianwei Shen, Yurong Chen, Long Quan, and Hongen Liao. Learning two-view correspondences and geometry using order-aware network. In *ICCV*, 2019. [7](#)
118. Xu Zhang, Felix X. Yu, Svebor Karaman, and Shih-Fu Chang. Learning Discriminative and Transformation Covariant Local Feature Detectors. In *The IEEE Conference on Computer Vision and Pattern Recognition (CVPR)*, July 2017. [2](#)
119. Chen Zhao, Zhiguo Cao, Chi Li, Xin Li, and Jiaqi Yang. NM-Net: Mining Reliable Neighbors for Robust Feature Correspondences. In *CVPR*, 2019. [3](#), [8](#)
120. Qunjie Zhou, Torsten Sattler, Marc Pollefeys, and Laura Leal-Taixe. To learn or not to learn: Visual localization from essential matrices. In *ICRA*, 2020. [2](#)
121. Siyu Zhu, Runze Zhang, Lei Zhou, Tianwei Shen, Tian Fang, Ping Tan, and Long Quan. Very Large-Scale Global SfM by Distributed Motion Averaging. In *CVPR*, June 2018. [2](#), [3](#)
122. C.L. Zitnick and K. Ramnath. Edge Foci Interest Points. In *ICCV*, 2011. [3](#)